

Review

Performance of Additively Manufactured Fuels for Hybrid Rockets

Calvin Nguyen and James C. Thomas *

J. Mike Walker '66 Department of Mechanical Engineering, Texas A&M University,
College Station, TX 77843, USA; calvinnguyennn@tamu.edu

* Correspondence: james.chris.thomas@tamu.edu

Abstract: Hybrid rocket engine (HRE) performance is dependent on fuel/oxidizer selection and fuel grain geometry. A literature review was performed to identify key trends and findings related to the application of the additive manufacturing (AM) of fuel systems for HREs. The effects of complex combustion port geometries, embedded structures, and end-burning systems, along with the use of metallic additives, turbulators, diaphragms, gel-like fuels, powdered fuels, liquid fuels, and liquifying fuels and their impact on regression rates, combustion efficiencies, and/or mechanical strength are thoroughly documented here. In general, the application of AM to HRE fuels can be implemented to increase regression rates and combustion efficiency, and tailor HRE designs. Chemical equilibrium analysis computations were completed to characterize the theoretical performance of HTPB and common AM fuels (ABS, PLA, PC, PMMA, Nylon 6, and a UV-based fuel) with common oxidizers (LOX and N₂O). AM fuels exhibit a similar theoretical performance as the commonly used HTPB fuel, and proper selection of the fuel can yield improved performance and design metrics. Development of AM approaches for HRE fuel design have significantly expanded their design trade space and should enable the competitive application of HREs for future propulsion missions.

Keywords: hybrid rocket; additive manufacturing; fuel; literature review; chemical equilibrium analysis



Citation: Nguyen, C.; Thomas, J.C.

Performance of Additively
Manufactured Fuels for Hybrid
Rockets. *Aerospace* **2023**, *10*, 500.
[https://doi.org/10.3390/
aerospace10060500](https://doi.org/10.3390/aerospace10060500)

Academic Editor: Hui Tian

Received: 30 April 2023

Revised: 16 May 2023

Accepted: 17 May 2023

Published: 25 May 2023

1. Introduction

Hybrid rocket engines (HREs) are chemical rockets with their fuel and oxidizer stored in different states of matter. The traditional hybrid rocket configuration is composed of a solid fuel and a liquid or gaseous oxidizer. In contrast, solid and liquid rockets entirely comprise solid or liquid fuels and oxidizers, respectively. Figure 1 shows a general schematic of solid, hybrid, and liquid propulsion systems. Compared to solid rocket motors (SRMs), HREs are throttleable, restartable, environmentally friendlier, and safer [1]. Compared to liquid rocket engines (LREs), HREs are mechanically simpler, environmentally friendlier, safer, have a larger variety of fuels, and are cheaper [1]. Despite the advantages of HREs, they are commercially used as often as SRMs and LREs due to some limitations, including low regression rates, lower combustion efficiencies, and a shift in oxidizer-to-fuel (O/F) ratio during combustion or throttling [1].



Copyright: © 2023 by the authors.
Licensee MDPI, Basel, Switzerland.
This article is an open access article
distributed under the terms and
conditions of the Creative Commons
Attribution (CC BY) license ([https://
creativecommons.org/licenses/by/
4.0/](https://creativecommons.org/licenses/by/4.0/)).

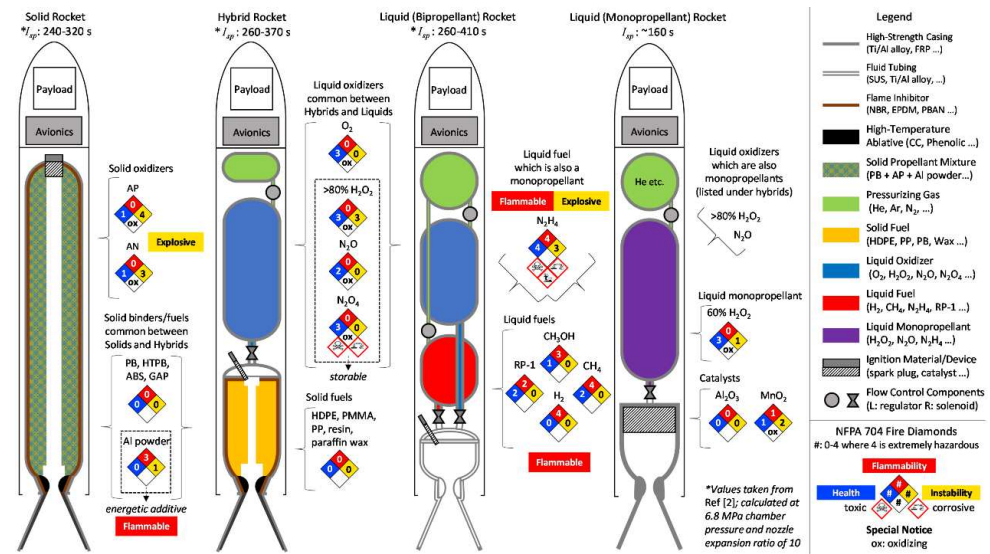


Figure 1. General framework and schematics of solid, hybrid, and liquid propulsion systems. Image reprinted from Ref. [2] with permission under the Creative Commons 4.0 License.

Hybrid rocket engines are commonly used in low thrust applications such as upper stage propulsion, satellite maneuvering, or CubeSat rideshares [1]. The low thrust in HREs is caused by low fuel regression rates which also make it difficult to practically scale up these systems to larger scales. Fuel grains must be extraordinarily long to produce large thrusts, but this approach results in poor volumetric efficiency and lateral structural issues. Factors that influence the fuel regression rates include operating pressure, temperature, fuel/oxidizer composition, grain geometry, O/F ratios, and oxidizer mass flow rate. Additive manufacturing (AM) has recently been used to increase regression rates by altering grain geometry and fuel composition. For example, the utilization of AM has resulted in a variety of enhancement methods including fuel grains containing complex port geometries, multiple fuels, and port arrays. Complex port geometries generate turbulence or provide additional burning surface area. Combinations of multiple fuels have been used to increase regression rates via liquid entrainment or increased surface area while simultaneously improving mechanical strength. Having an array of small ports can yield an end-burning phenomenon where the fuel regresses axially. These methods and their effectiveness are discussed in greater depth within the literature review. A broader review of additively manufactured hybrid rocket fuels and components with respect to printing processes is provided by Oztan and Coverstone [3]. The remainder of this section is dedicated as an introduction to basic additive manufacturing methods and ballistic characterization techniques for hybrid rocket fuels.

1.1. Introduction to Additive Manufacturing

Additive manufacturing is a broad term referring to the process of printing successive layers on top of each other to fabricate a product. Models are developed in computer-aided design (CAD) software which are digitally sliced into layers and subsequently printed. The additive nature results in low waste and minimal need for post-processing. Many materials can be printed, including polymers, metals, ceramics, or biomaterials, in the form of liquid, filament/paste, powder, or solid sheet [4]. Additive manufacturing is particularly interesting for HRE applications because of the ability to fabricate structures with complex geometries that cannot be manufactured with traditional subtractive methods or casting. The final product's mechanical properties depend on various factors, including AM technique, selected material, extrusion pressure, filament orientation, laser power, layer thickness, printing direction, printing temperature, and printing speed [5]. However, AM generally results in an increased porosity which yields a reduction in mechanical strength and density [5]. Additive manufacturing includes many different printing techniques, but

an emphasis will be placed on fused deposition modeling (FDM), selective laser sintering (SLS), and stereolithography (SLA) due to their relevance to HREs. A diagram of each of these AM methods is provided in Figure 2.

Fused deposition modeling is the most common AM method used because of its low cost, high speed, and simplicity [5]. Figure 2a illustrates the FDM printing process where a polymer in the form of a filament is heated near its melting temperature and extruded through a nozzle. The polymer leaves the nozzle in a semi-liquid state and is deposited in successive layers. The polymer solidifies and fuses with previous layers upon reaching room temperature. Typical materials include thermoplastics such as acrylonitrile butadiene styrene (ABS), polylactic acid (PLA), acrylic, and nylon. Mechanical properties of the printed product are dependent on layer thickness, width, filament orientation, and air gap between layers [6]. Products printed using FDM typically suffer from weak mechanical properties, layer-by-layer appearance, and poor surface quality [7].

Selective laser sintering is a powder-based method that prints products using a laser. Figure 2b illustrates the SLS printing process where a powdered bed is heated just below melting temperatures, and a laser beam sinters particles into a desired 2D shape [4]. The powder bed is then lowered, and a new layer of powder is laid on top. The strength and density of the printed product largely depend on particle size and distribution [4]. Common materials used in SLS include polymers, metals, and alloys. SLS techniques produce prints with good mechanical properties [4] and fine resolution but are comparatively slower than FDM methods [5].

Stereolithography utilizes liquid materials such as photopolymer resins which are permeable and curable by an ultraviolet (UV) laser. Figure 2c illustrates the SLA printing process where a UV laser is precisely directed along the photopolymer resin to create a solid layer by photopolymerization. The base plate is subsequently lowered by a height of the desired layer thickness, and a new layer of liquid floods the surface. The part is heat-treated after printing inside of an oven or with a photocuring process to enhance mechanical properties [4]. SLA produces high-quality prints with a resolution as good as $10\ \mu\text{m}$ [8]. However, SLA is slow, mechanically weak, has limited printing materials, and may experience shrinkage or warping [4]. SLA is typically utilized in end-burning HREs due to the requirement of small, accurate, and consistent port diameters.

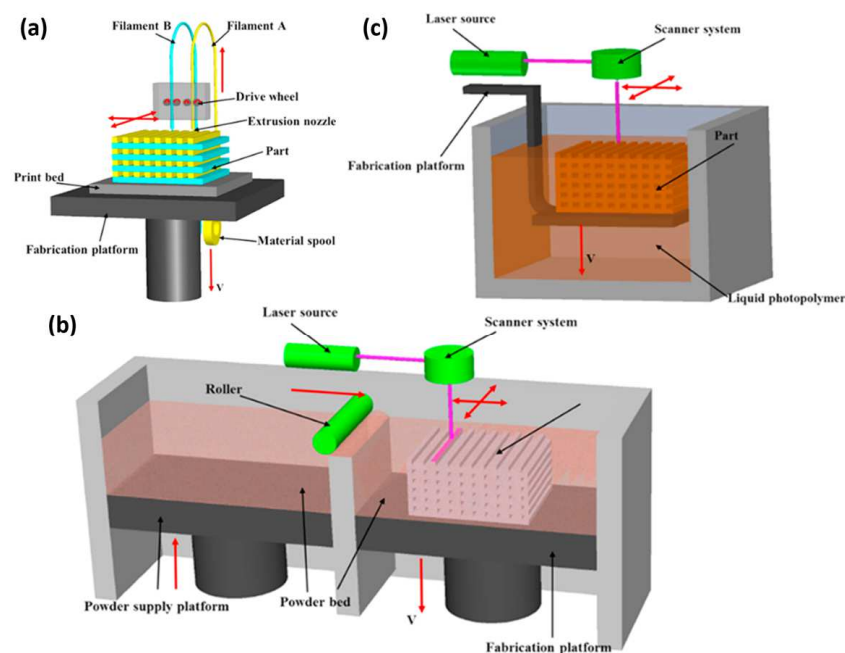


Figure 2. Additive manufacturing methods: (a) fused deposition modeling; (b) selective laser sintering; (c) stereolithography. Image reprinted from Ref. [9] with permission from Elsevier.

1.2. Ballistic Performance

Hybrid rocket propellants undergo a boundary layer combustion process where a diffusion flame region forms inside the combustion port, as shown in the simplified schematic of Figure 3. The flame zone delivers heat to the fuel grain through convection and radiation heat transfer which causes surface fuel pyrolysis and corresponding fuel mass flow into the oxidizer stream where the combustion reaction occurs. However, when the fuel surface ablates, it causes a blowing effect due to an increase in the thickness of the boundary layer and a reduction in heat transfer to the surface.

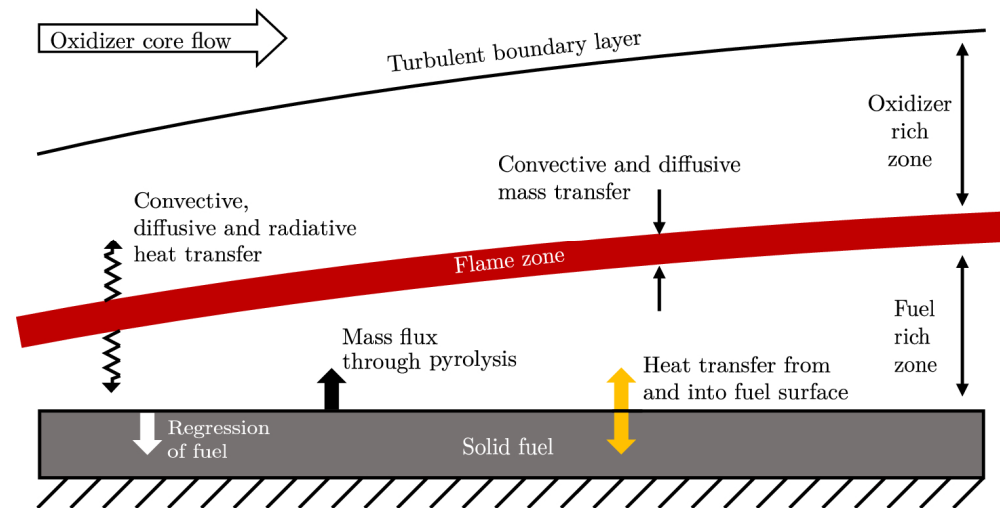


Figure 3. Boundary layer combustion process for HREs through mass pyrolysis. Image reprinted from Ref. [10] with permission under the Creative Commons 4.0 License.

The fuel regression rate is the rate at which the solid fuel burns normally to the burning surface. The regression rate (\dot{r}) is one of the most important metrics used to assess propellant performance and can be theoretically modeled by the Marxman analysis:

$$\dot{r} = 0.036 \frac{G^{0.8}}{\rho_f} \left(\frac{\mu}{x} \right)^{0.2} \beta^{0.23} \quad (1)$$

where G is the total free-stream propellant mass velocity at any given axial combustion port location (x), ρ_f is the fuel density, μ is the combustion gas viscosity, and β is the blowing coefficient [11]. However, Equation (1) is commonly simplified to Equation (2) for experimental measurements:

$$\bar{\dot{r}} = a G_{ox}^n \quad (2)$$

where $\bar{\dot{r}}$ is the average regression rate of the entire fuel grain, G_{ox} is the oxidizer mass flux, and a and n are empirically fitted constants. Equation (2) assumes that the regression rate is uniform along the grain length and is not dependent on pressure. The empirical constants (a and n) are strongly dependent on facility effects, such as combustor design, measurement approach, etc. Results from Equation (1) begin to diverge from experimental results at low and high mass flow rates due to an increased dependency on pressure, radiative heat transfer, or chemical kinetics [12]. Figure 4 illustrates the various regression rate regimes and key dependencies where most HREs operate in the middle regime dominated by turbulent heat transfer processes.

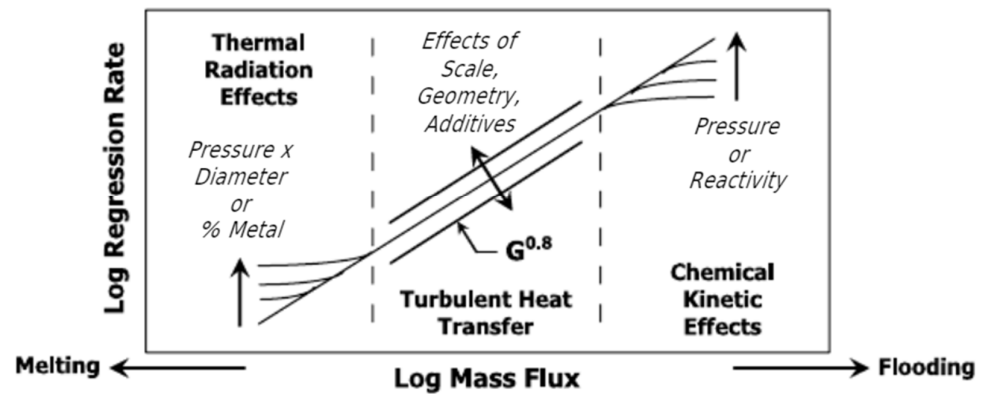


Figure 4. Regression rate regimes and parameter dependencies for HREs. Image reprinted from Ref. [13] with permission from AIAA.

The performance of fuel grains is commonly evaluated using lab-scale motors, as shown in Figure 5a. Instantaneous measurements of regression rates are complex and difficult to implement, so they are not generally performed when using lab-scale motors. Instead, time- and space-averaged methods are used for cylindrical ports. The two most common methods for approximating regression rates include a mass-based and geometry-based method. The mass-based method is given by:

$$\dot{r}_{MB} = \frac{\Delta m_f}{\rho_f A_{b,avg} \Delta t_b} \quad (3)$$

where Δm_f is the difference in fuel mass before and after combustion, ρ_f is the fuel density, $A_{b,avg}$ is the average burning area, and Δt_b is the combustion time. The geometry-based method is given by:

$$\dot{r}_{GB} = \frac{D(t_f) - D(t_0)}{2 \Delta t_b} \quad (4)$$

where $D(t_f)$ and $D(t_0)$ are the final and initial port diameters, respectively.

Alternative methods to evaluate fuel performance include using 2D slab burners and ladder-shaped resistors. Two-dimensional slab burners (Figure 5b) are optically accessible and allow for instantaneous measurements of fuel regression and flow visualization. However, the geometry of the fuel slab and side-burning effects can alter the observed fuel performance. Ladder-shaped resistors have been used by Ozawa et al. [14] amongst others for on-board and real-time fuel regression measurements. Multi-material AM is utilized to print the ladder-shaped resistors into the fuel grain. Fuel regression is measured from the detection of step voltages caused by rung breakage in the ladder as the fuel regresses. Figure 5c shows the ladder resistor structure implemented into a single-port fuel grain.

Another important indicator of fuel performance is combustion efficiency. The combustion efficiency (η) is generally defined as the ratio of experimental and theoretical characteristic velocities:

$$\eta = \frac{c_{exp}^*}{c_{th}^*} \quad (5)$$

where c_{exp}^* and c_{th}^* are the experimental and theoretical characteristic velocities, respectively. The experimental characteristic velocity is determined from measurements taken during HRE firings:

$$c_{exp}^* = \frac{P_c A_t}{\dot{m}} \quad (6)$$

where P_c is the chamber pressure, A_t is the nozzle throat area, and \dot{m} is the total mass flow rate. Similar to the experimental regression rate, average properties are generally used to

compute experimental characteristic velocities. The theoretical characteristic velocity is calculated using chemical equilibrium analysis (CEA) and is given by:

$$c_{th}^* = \sqrt{\frac{RT_{AF}}{\gamma} \left(\frac{\gamma + 1}{2} \right)^{\frac{\gamma+1}{\gamma-1}}} \quad (7)$$

where R is the specific gas constant, T_{AF} is the adiabatic flame temperature, and γ is the specific heat ratio for the product gases.

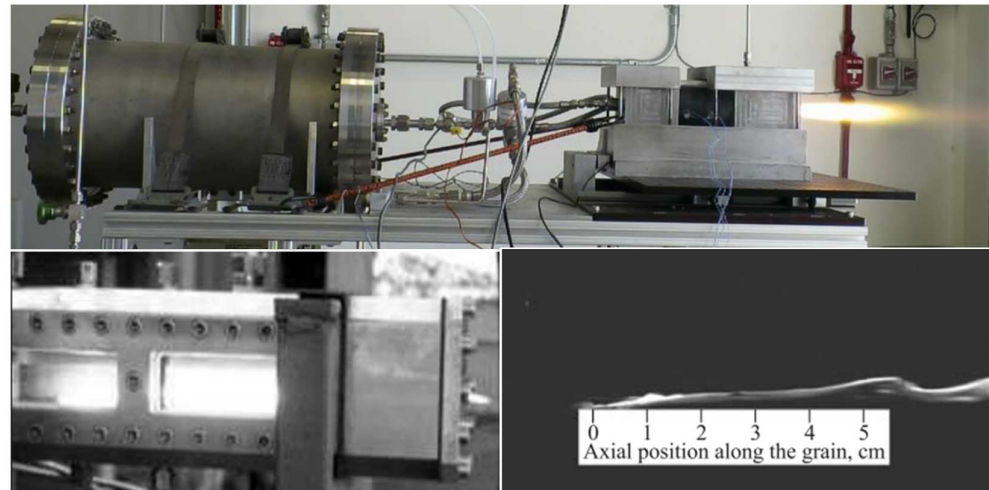


Figure 5. Methods utilized to evaluate fuel performance: (top) representative lab-scale cylindrical motor [15] and (bottom) 2D slab burner [16]. Images reprinted from Refs. [15,16] with permission under the Creative Commons 4.0 License.

1.3. Outline of Present Work

In the following section, the experimental effects of AM on hybrid rocket fuels are reviewed, with an emphasis on fuel performance. An extensive compilation of printed fuel grains and relevant data from the literature is presented to introduce the impact of novel techniques. In the subsequent section, performance predictions of common printable fuels are calculated using CEA. Finally, a summary of the literature and future trends are summarized in the conclusion section.

2. Literature Review of Additive Manufacturing in Hybrid Rockets

2.1. Comparison of Printed Fuels

Hydroxyl-terminated polybutadiene (HTPB) is a thermosetting polymer and is the most common fuel used for HREs due to its industry familiarity and safety. HTPB's components must undergo a relatively complex casting and curing process with approximately two weeks of production time to yield the fully cured fuel system [17]. Alternative fuels which utilize AM have been explored due to the casting nature and long production times of HTPB. Using AM to produce fuel grains is generally simpler and faster than casting methods and provides the ability to produce unique and complex grain geometries. Additive manufacturing has also been utilized to print water-soluble casting molds with complex geometries [18].

ABS is one of the most commonly used AM thermoplastics for general printing purposes and with the HRE community. Whitmore et al. [17] compared the performance of ABS and HTPB fuel grains with identical geometries. Static fire tests with nitrous oxide were performed in a test cell housed at Utah State University. ABS exhibited a slightly lower overall performance in comparison to HTPB but was significantly more consistent. The combustion efficiency, steady-state thrust, specific impulse, and equivalent vacuum specific impulse of the HTPB grains were approximately 3%, 5%, 4.2%, and 4.1% greater

than the ABS grains', respectively [17]. The HTPB grains also exhibited a slightly higher regression rate than the ABS grains. The authors attributed the slightly lower performance of the ABS grains to its higher heat of gasification and higher enthalpy, resulting in a lower plume temperature and lower energy burn [17]. Overall, ABS and HTPB have a very similar ballistic performance. However, ABS has a significantly higher tensile strength (40 MPa) than HTPB (800 kPa) which makes it less susceptible to grain fracture [19]. In addition, ABS has also been shown to contain electrical arcing properties which allows for multiple restart capabilities with relatively low voltages (200–300 V) [20].

Yu et al. [21] investigated the performance of printed ABS with varying levels of packing density, or infill, ranging from 60–100% along with a solid ABS grain, which was developed using a subtractive manufacturing method (computer numeric control (CNC) lathe). The authors present two burning regimes which were caused by a penetrative combustion mechanism. Decreasing the packing density resulted in significant increases in fuel regression rates, as shown in Figure 6. The grains in the normal layer-by-layer combustion regime (90%, 100%, and solid) experienced steady increases in regression rates as the oxidizer mass flux increased. The grains in the shattered volumetric combustion regime (60–80%) experienced sharp increases in regression rates as the oxidizer mass flux increased. It should be noted that the regression rates were measured using a weight difference method which is less accurate than thickness over time methods. The 100% packing density printed ABS grain also contained void spaces due to printer error, unlike the solid fuel grain developed from subtractive manufacturing methods.

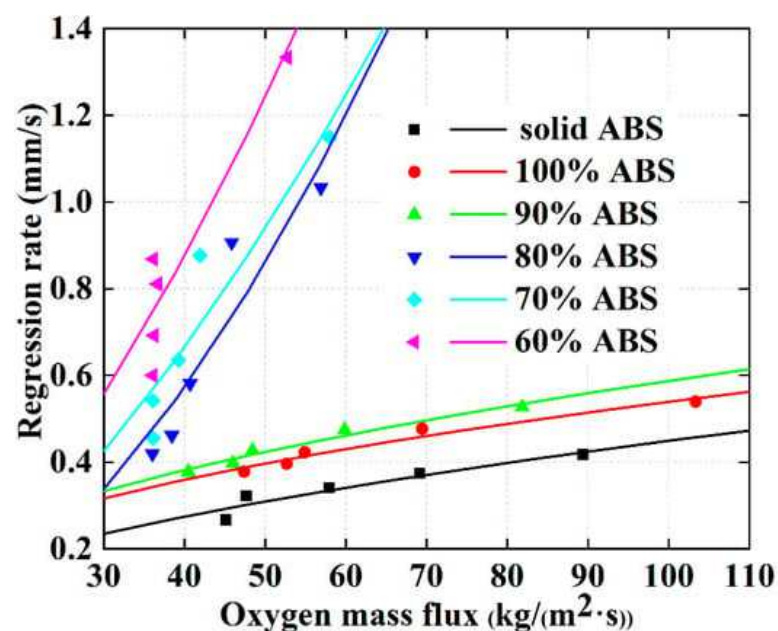


Figure 6. Firing results of ABS with packing densities between 60–100% along with a solid grain developed from a CNC lathe. Image reprinted from Ref. [21] with permission under the Creative Commons 4.0 License.

McFarland and Antunes [22] investigated the fuel performance of various thermoplastics produced using FDM. The thermoplastics evaluated included ABS, acrylonitrile styrene acrylate (ASA), PLA, polypropylene (PP), polyethylene terephthalate glycol (PETG), and nylon. Small-scale single motor firings were performed on two fuel grains of each material with the same geometry. Cross sections of the fuel grains after firing are shown in Figure 7. ASA, nylon, PP, and PLA exhibited regression rates that were 51.4%, 43.8%, 17.1%, and 17.1% greater than ABS, respectively [22]. PETG exhibited regression rates that were 10.5% lower than ABS; however, its burn temperature was significantly hotter than the other materials. It should be noted that the printing settings were adjusted throughout

the manufacturing process, resulting in some fuel grains containing different geometrical defects which can affect fuel performance.



Figure 7. Cross section of the small-scale fuel grains after firing, left to right: ABS, PLA, PP, ASA, and PTEG. Image reprinted from Ref. [22] with permission under the Creative Commons 4.0 License.

These studies demonstrate there is a design trade space for fuel selection within AM HREs. The regression rate, density, and ballistic properties of a standard cylindrical HRE can be tailored by the selection of AM thermoplastics. However, characterization of the ballistic properties of such fuels over a range of conditions (oxidizer mass flux, O/F, pressure, etc.) should be conducted to fully elucidate the potential of individual fuels. ABS is the only thermoplastic AM fuel that has been thoroughly characterized to date.

2.2. Complex Combustion Port Geometries

The use of complex combustion port geometries is a novel method made possible due to recent developments in additive manufacturing. Complex port geometries provide additional burning surface area or generate turbulence through complex flow patterns which cause an increase in regression rates. The swirling flow of fuel and oxidizer pushes the flame zone closer to the burning surface which increases the flame diffusion efficiency and thus increases fuel regression rates. Manipulating the flow stream is preferred instead of using high oxidizer mass fluxes which can cause combustion instability, nozzle erosion, and increase the O/F ratio. Changing the O/F ratio drives the combustion reaction away from its stoichiometric point and reduces the fuel's combustion efficiency. The traditional method to calculate average regression rates cannot be used on complex port geometries due to the non-circular port shapes. Various methods are used to calculate regression rates within this section which result in differences between the reported regression rates.

2.2.1. Helical Ports

Helical ports (Figure 8) are used to increase regression rates by introducing a centrifugal flow pattern and lengthening the internal flow path. The centrifugal flow pattern enhances the surface skin friction and thins the wall boundary layer which results in a decrease in the blowing effect and an increase in the convective heat transfer to the burning surface. The longer internal flow path increases the burning surface area. The helical structure is defined by three components: fuel port diameter, loop diameter, and pitch length, as illustrated in Figure 8. The radius of curvature increases as the burn-time of the fuel grain increases which causes the fuel port to become more cylindrical and the regression rate enhancements to diminish.

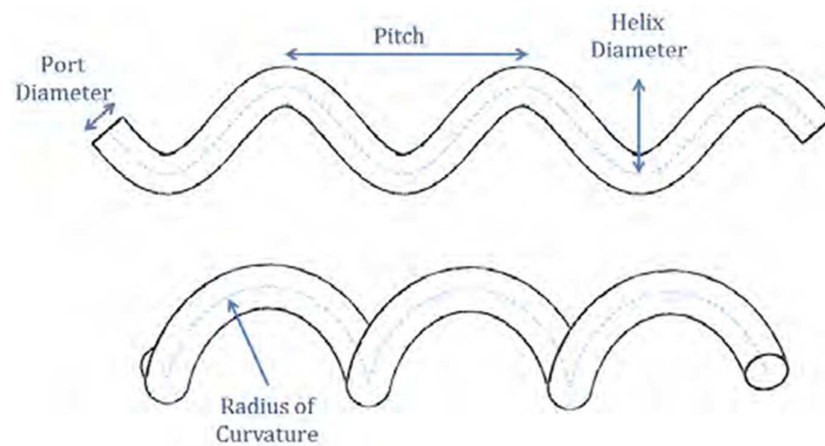


Figure 8. Characteristics of a helical fuel port. Image reprinted from Ref. [19] with permission from AIAA.

Walker [19] investigated the effects of a helical port in ABS grains fired with GOX, as shown in Figure 9. Some fuel grains with the helical port experienced regression rate increases greater than a factor of three compared to identical grains with a straight port [19]. Helical ports with a short pitch length experienced the highest initial regression rate increase but also showed the greatest regression rate drop-off as the port became more cylindrical. The grains with helical ports also had significantly lower O/F ratios than their straight port counterparts due to the longer port lengths.

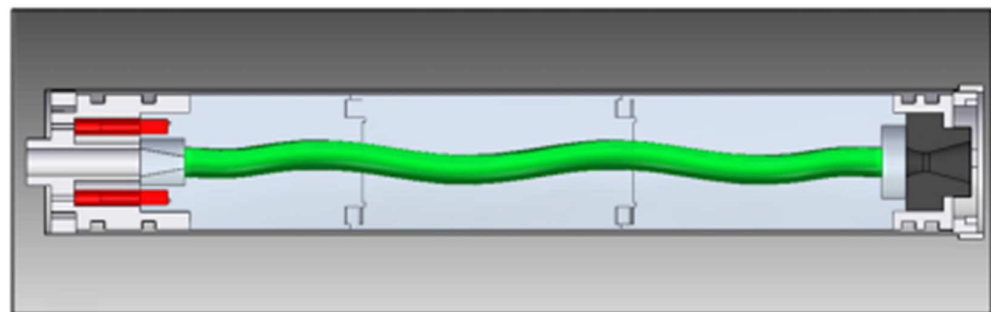


Figure 9. Schematic of helical fuel grain evaluated by Walker [19]. Image reprinted from Ref. [19] with permission from AIAA.

Wang et al. [23] tested a nested helical structure embedded with a paraffin-based fuel. The helical structure was printed from ABS (14 wt.%), and the embedded paraffin (86 wt.%) contained additives such as Ethylene Vinyl Acetate Copolymer (EVA), stearic acid, and carbon powder. Figure 10 shows the concept and components of the novel grain. The performance of the novel fuel grain was compared to an identical fuel grain made from pure paraffin-based fuel using lab-scale firings with GOX. The nested structure increased the average regression rate by approximately 20% and slightly increased the combustion efficiency when compared to the pure paraffin-based fuel grain [23]. The novel fuel grain performed the best at high oxidizer mass fluxes and showed no significant changes in performance from fuel grain cracks or changes in chamber pressure with mass flow rates between 9.5–19 g/s. The authors believe that the increased performance is due to the induced swirling from the nested structure which causes an increase in fuel and oxidizer mixing and creates recirculation zones. It should be noted that the ABS used in this study had a lower ballistic performance than traditional ABS due to the addition of flame retardants.

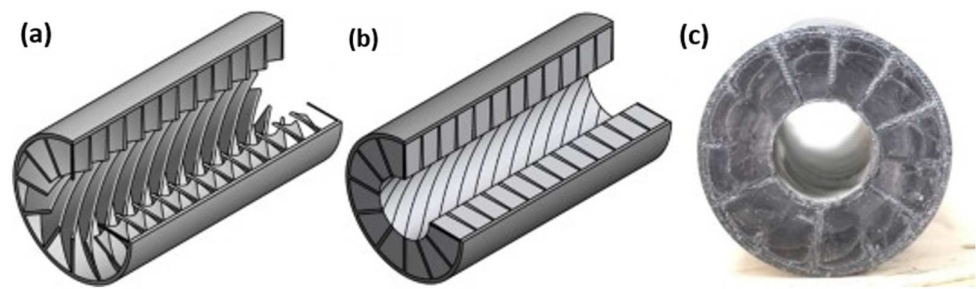


Figure 10. Concept of the nested helical structure tested by Wang et al.: (a) ABS structure; (b) nested structure filled with paraffin-based fuel; (c) photographic image of the grain. Image reprinted from Ref. [23] with permission from Elsevier.

Zdybal et al. [24] combined the concept of an armored grain with complex port geometries by investigating the performance of an FDM-printed polyamide-12 skeleton grain (10% infill) impregnated with polyethylene wax containing 5% EVA with a helical port geometry. Figure 11 illustrates the printed skeleton structure and the fuel grain after testing. The primary intent of this study was to determine the effects of pitch length on fuel performance. A decrease in pitch length caused regression rates to increase by up to 26.7% and the corresponding combustion efficiency to decrease by 34% compared to an identical straight port grain [24]. The significant decrease in combustion efficiency is believed to be attributed to an insufficient length of the post-combustion chamber. This study only presents preliminary results as only one test was performed for each fuel grain configuration. The authors also experienced multiple problems throughout the experimental process regarding their oxidizer tank, pressure measurements, and electronic systems, which affected the experimental results.

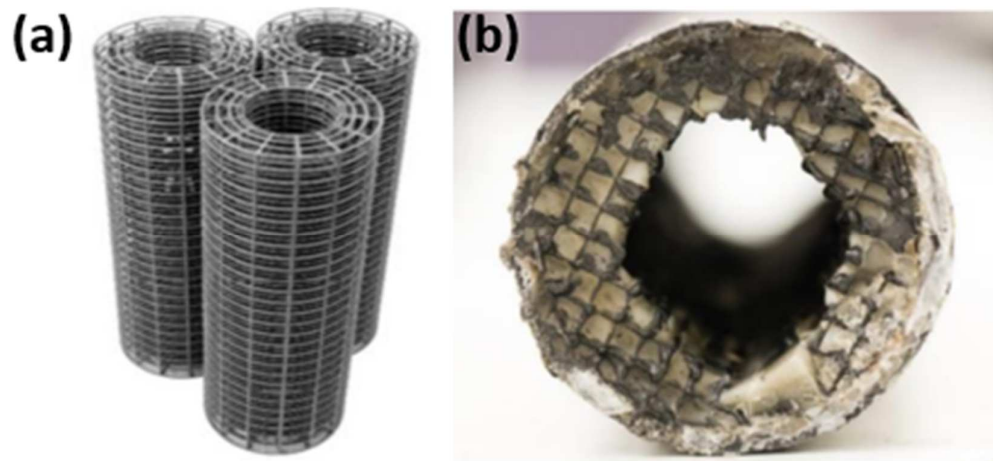


Figure 11. Fuel grains investigated by Zdybal et al. which combine the concepts of the armored grain and complex port geometries: (a) skeleton structure; (b) photograph of burned fuel grain. Images reprinted from Ref. [24] with permission from AIAA.

Tian et al. [25] investigated the effects of thread pitch, groove depth, and groove width on helical fuel grains. Figure 12 shows a schematic of the fuel grain and motor tested. Lab-scale firings were performed with polyethylene and GOX with thread pitches between 18–30 mm, groove depths between 2–6 mm, and groove widths between 8–12 mm. A decrease in thread pitch, increase in groove depth, and increase in groove width resulted in increased average regression rates by 40%, 15–20%, and 10%, respectively, for the dimensions tested [25].

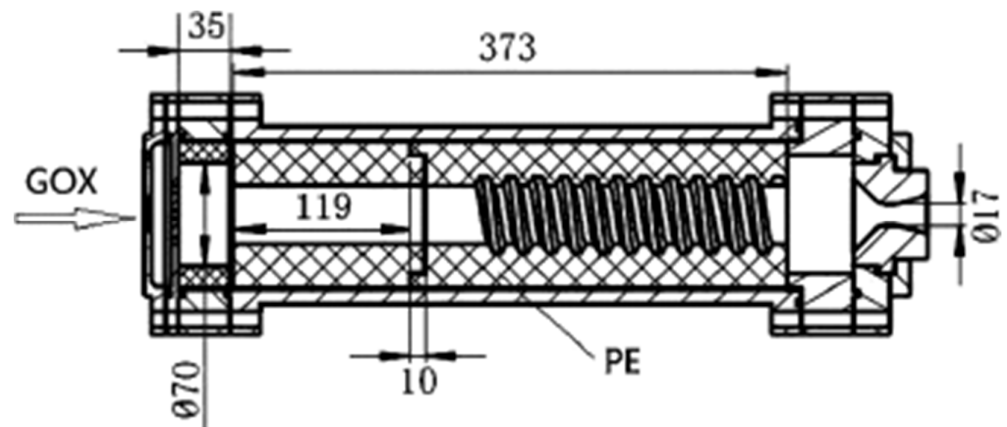


Figure 12. Schematic of hybrid rocket motor configuration tested by Tian et al. [25] to investigate the effects of thread pitch, groove depth, and groove width. Image reprinted from Ref. [25] with permission from Elsevier.

2.2.2. Swirling Ports

Swirling ports differ from helical ports by twisting and running straight through the fuel grain instead of creating circular loops through it. Swirl ports increase average regression rates by imparting a swirling motion to the oxidizer flow which increases the turbulence and mixing of the oxidizer with the fuel. Swirl ports are characterized by their number of turns-per-inch (tpi) which influences fuel performance.

Arnold [26] tested fuel grains with a six-pointed star-swirl port containing turning angles of 1/8-, 1/4, and 1/2-tpi. The grains were printed from acrylic and fired with GOX. The 1/8, 1/4, and 1/2-tpi grains showed an average regression rate increase of 60%, 180%, and 250%, respectively, compared to straight cylindrical grains [26]. These results demonstrate a clear relationship between regression rate and tpi.

Yenawine [27] investigated the effects of star-swirl ports with 1/2-tpi in ABS grains fired with GOX. The performance of fuel grains with star-swirl ports were compared to fuel grains with straight ports, as shown in Figure 13. The fuel grains were burned for approximately 10 s which resulted in the star-swirled port regressing into a cylindrical port. The star-swirl port increased the average regression rate by 36% over the straight cylindrical port when calculated using a mass-based method [27]. However, the star-swirled port also resulted in a decrease in combustion efficiency by 6.4% [27]. A limited number of tests were performed but similar results were demonstrated by McKnight et al. [28] where they implemented star-swirl ports with 1/2-tpi into fuel grains made from ABS (natural, white, and black) and Windform XT 2.0. The star-swirl port caused an increase in regression rates with all materials tested. The combustion efficiency of ABS grains similarly decreased, but the combustion efficiency of Windform XT 2.0 grains increased.

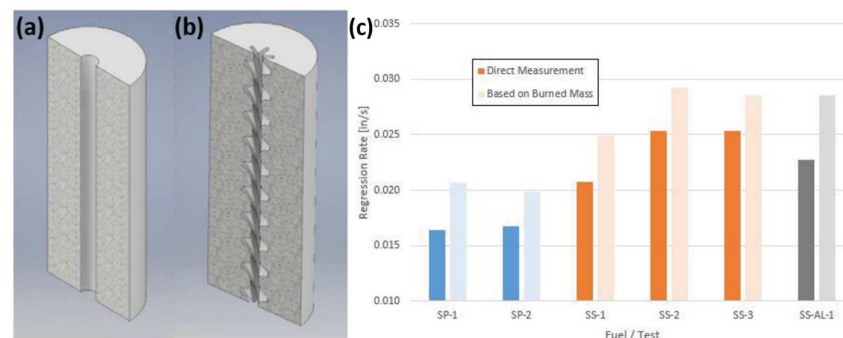


Figure 13. Comparison of geometry and performance between straight port (SP) and star-swirl (SS) fuel grains: (a) straight port design; (b) star-swirl design; (c) regression rate comparison with relatively similar oxidizer mass fluxes. Image reprinted from Ref. [27] with permission.

Young et al. [29] printed poly(methyl methacrylate) (PMMA) fuel grains containing a straight elliptical port and a swirl-elliptical port. The performance of these grains was compared to straight cylindrical grains using firing tests with GOX. The straight elliptical port showed no significant changes in regression rate or combustion efficiency, but the swirl-elliptical port showed an increase in regression rates and combustion efficiency by 35% and 10%, respectively [29].

Connell et al. [30] tested fuel grains made from polycarbonate (PC) and PMMA with multiple unique port geometries, including ramped protrusions, swirled-slotted, and swirl-ellipse, along with expansion and pocket modifications, as shown in Figure 14. Pitch lengths between 11.4 and 15.2 cm were tested for the swirl ports, and nominal GOX mass flow rates of either 15 or 30 g/s were imprinted. Only the effects from the port geometries are presented here due to the large number of testing parameters. Compared to a cylindrical port fuel grain, the ramped protrusion port decreased regression rates by 32–36% and had little effect on the combustion efficiency. The swirled-slotted port exhibited indifferent effects on regression rates ranging between -13% and $+43\%$ but increased the combustion efficiency by 0.6–6.6%. The swirl-ellipse grain increased regression rates by 64–116% and the combustion efficiency by 1.8–9.9%. The expansion region increased regression rates and combustion efficiency by 21% and 9%, respectively, while the pockets decreased regression rates by 8% and increased combustion efficiency by 7.4% [30]. It should be noted that regression rate measurements were taken from the exit of the fuel grain and a limited number of tests were performed.

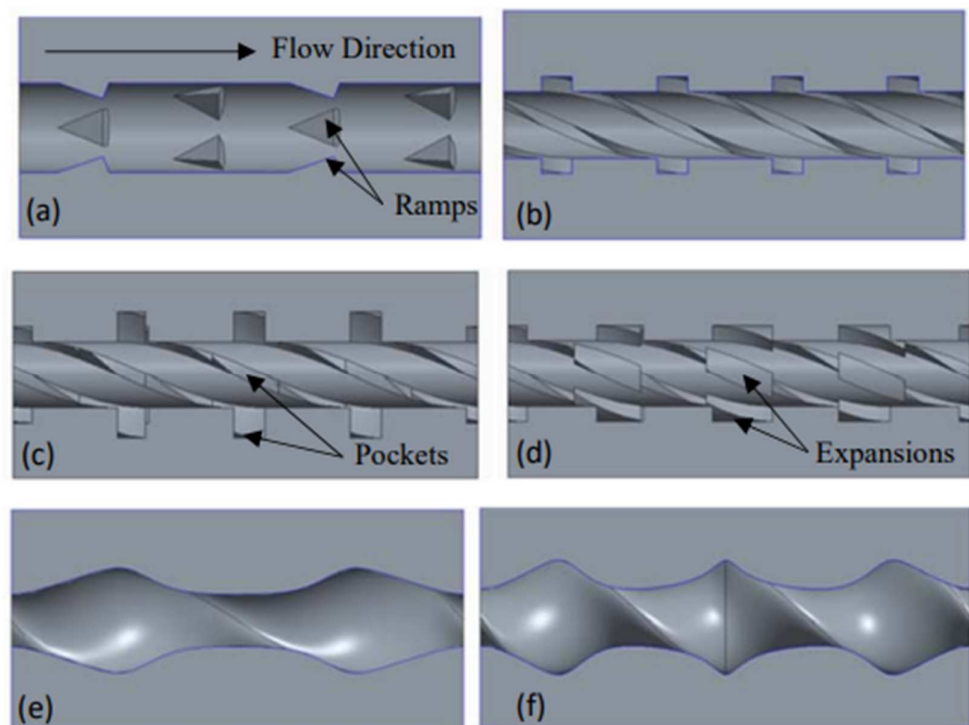


Figure 14. Sectioned views illustrating the internal flow geometries, including: (a) ramped protrusions; (b) swirl-slotted; (c) swirl-slotted with pockets; (d) swirl-slotted with expansions; (e) swirl-ellipse; (f) swirl-ellipse. Image reprinted from Ref. [30], is declared a work of the U.S. government, and is not subject to copyright protection in the United States.

2.2.3. Complex Combustion Port Geometries Summary

In this section, the effects of complex combustion port geometries on fuel performance are explored, and the results are summarized in Table 1. The ports discussed include helical and swirling ports with cylindrical, elliptical, or star shapes. The materials tested include ABS, PMMA, PC, acrylic, polyamide-12, Windform XT 2.0, paraffin, and polyethylene

wax. The regression rate of helical ports exhibited the best performance with short pitch lengths, but the O/F ratio significantly decreased, and the reported effects on combustion efficiency were disparate. The regression rates of swirling ports significantly increased with an increase in tpi, but the swirling effects on combustion efficiency were also disparate. It should be noted that different methods of calculating regression rates were utilized between studies which makes direct comparison difficult.

Table 1. Summary of results in the Complex Combustion Port Geometries section.

Reference	Geometry	Fuel	Oxidizer	Key Results
Walker [19]	Helical Port	ABS	GOX	Over 200% increase in RR Lower O/F ratios Shorter pitch length caused higher RR
Wang et al. [23]	Nested Helical Structure	ABS + Paraffin w/ additives	GOX	~20% increase in RR Slight increase in CE
Zdybal et al. [24]	Helical Port	Polyamide-12 + PEWAX w/ EVA	GOX	Up to 26.7% increase in RR Up to 34% decrease in CE Shorter pitch length caused higher RR
Tian et al. [25]	Helical Port	Polyethylene	GOX	Decreased thread pitch increased RR by 40% Increased groove depth increased RR by 15–20% Increased groove width increased RR by 10%
Arnold [26]	Six-pointed Star-Swirl Port	Acrylic	GOX	1/8 tpi: 60% increase in RR 1/4 tpi: 180% increase in RR 1/2 tpi: 250% increase in RR
Yenawine [27]	Star-Swirl Port 1/2 tpi	ABS	GOX	36% increase in RR 6.4% decrease in CE
McKnight et al. [28]	Star-Swirl Port 1/2 tpi	ABS (natural, white, black) and Windform XT 2.0	GOX	All materials increased in RR ABS decreased in CE Windform XT 2.0 increased in CE
Young et al. [29]	Straight Elliptical Port	PMMA	GOX	No significant change in RR or CE
Young et al. [29]	Swirl-Elliptical Port	PMMA	GOX	35% increase in RR 10% increase in CE
Connell et al. [30]	Ramped Protrusion Port	PC or PMMA	GOX	32–36% decrease in RR No significant change to CE
Connell et al. [30]	Swirled-Slotted Port	PC or PMMA	GOX	–13% to +43% change in RR 0.6–6.6% increase in CE Expansion region: 21% increase in RR, 9% increase in CE Pockets: 8% decrease in RR, 7.4% increase in CE
Connell et al. [30]	Swirl-Ellipse Port	PC or PMMA	GOX	64–116% increase in RR 1.8–9.9% increase in CE

Abbreviations: RR, Regression Rate; CE, Combustion Efficiency.

2.3. Multi-Fuel Printed Systems

Multi-fuel printed systems are fuel grains that utilize multiple propellants and are produced using AM. A high-regression-rate fuel is paired with a ‘structural’ fuel due to its poor mechanical properties and inability to form a fuel grain by itself. Fuels with high regression rates include liquifying fuels or powdered fuels due to the entrainment phenomenon and high surface area, respectively. Structural fuels include thermoplastics or metals such as PLA, ABS, or aluminum (Al).

Liquifying fuels (paraffin wax) are characterized by their trait of melting prior to vaporizing. A thin liquid layer forms on the surface of the solid fuel within the turbulent boundary layer. As the oxidizer flows across the surface, liquid droplets are sheared from the liquid layer and entrained into the oxidizer stream. The liquid droplet then vaporizes and adds energy to the system proportional to the entrainment rate (\dot{m}_{ent}):

$$\dot{m}_{ent} \approx \frac{P_d^\alpha h^\beta}{\mu_f^\gamma \sigma_f^\pi} \quad (8)$$

where P_d is the dynamic pressure, h is the liquid layer thickness, μ_f is the liquid fuel layer viscosity, σ_f is the liquid fuel surface tension, and the superscripts α , β , γ , π are empirical constants. Karabeyoglu et al. [31] suggested the melt layer viscosity plays a more important role than the surface tension ($\gamma > \pi$) in entrainment mass transfer and the superscript values α and β range from 1–1.5. They also suggest that the total regression rate is the sum of the vaporization and entrainment regression rates [31]. Liquifying fuels have exhibited regression rates three to four times that of conventional hybrid fuels due to the entrainment phenomenon [32]. However, liquifying fuels are brittle and experience “sloughing”, which is where chunks of unburned fuel are expelled from the HRE before fully combusting and results in decreased combustion efficiencies. The effects from sloughing have been shown to increase at elevated temperatures [33].

2.3.1. Paraffin Additives

Additives are commonly mixed into paraffin to improve mechanical properties such as tensile strength, yield strain, or elastic modulus due to its inherent brittleness. Although there are no AM techniques directly employed when making these paraffin fuel blends, the additives significantly impact fuel performance, so a brief introduction will be presented. Styrene-Ethylene-Butylene-Styrene Copolymer grafted with Maleic Anhydride (SEBS-MA) [34], EVA [34–39], Low-Density Polyethylene (LDPE) [35,38], polypropylene (PP) [38], and High-Density Polyethylene (HDPE) [38] are all additives to paraffin which improve mechanical properties but decrease regression rates. Stearic acid has been shown to improve mechanical properties with an increase [38] or no effect [37] on regression rates. Nano-aluminum powder, Magnesium Hydride, and Lithium Aluminum Hydride have all demonstrated an increase in regression rates, but no mechanical tests were performed [40].

2.3.2. Embedded Structures

At the Space Propulsion Lab (SPLab) of Politecnico di Milano, Bisin et al. [41–45] embedded an FDM-printed reinforcing structure into paraffin wax and named it the armored grain, as shown in Figure 15. The rationale of the armored grain is to improve the mechanical properties of the paraffin-based fuel grain without hindering regression rates. The effects of geometry (gyroid, Schwarz P, straight honeycomb, and twisted honeycomb) [44], printing material (PLA, ABS, NY) [41], and infill (0, 10, 15 vol.%) [43] of the embedded structure along with wax type (micro- and macro-crystalline) [43] and wax additive (0, 5, 10 wt.% SEBS-MA) [43] were investigated. Figure 16 illustrates the various grain structures printed. Mechanical and ballistic properties were determined using uniaxial compression tests and lab-scale HRE firings. The armored grain generally decreased or had no effect on the Young’s modulus, increased the yield stress, and increased the yield strain when compared to pure paraffin grains [42,43,45]. The addition of the embedded structure also caused the paraffin-based fuel grain to turn from brittle to ductile [42], provided better mechanical improvements than some paraffin additives [42], and increased regression rates when compared to pure paraffin [41]. The gyroid shape represented a good compromise between ballistic and mechanical properties, while the Schwarz P had the greatest regression rates but lowest mechanical strength [44]. The geometries studied have shown to increase regression rates by 16–36% and 167–264% when compared to pure paraffin and HTPB, respectively [44]. ABS demonstrated the highest regression rates of the evaluated

materials used to construct the embedded structure [41]. An increase in infill percentage generally resulted in a decrease in regression rates, but an increase in mechanical properties and ductility [43]. Macro-crystalline wax exhibited higher regressions rates and lower mechanical strength than micro-crystalline wax [43]. The addition of SEBS-MA caused increases in strength and stiffness but reduced regression rates [43]. The authors believe that the rough embedded structure causes an increase in convective heat transfer which resulted in increased regression rates experienced by the armored grains [41].

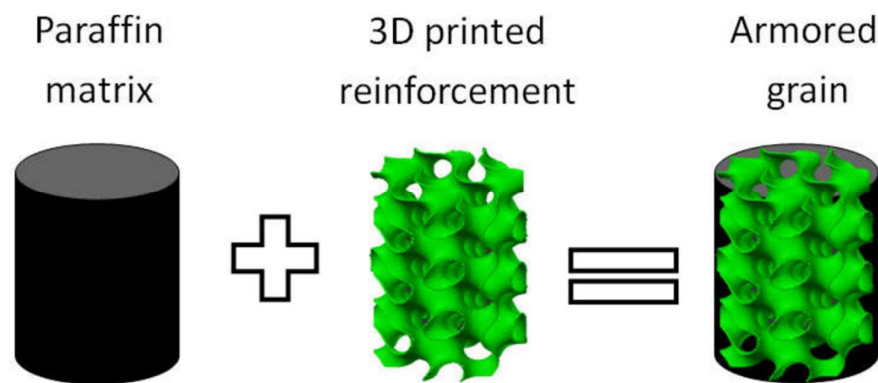


Figure 15. Armored grain concept exploiting 3D printed gyroid reinforcement. Image reprinted from Ref. [44] with permission.

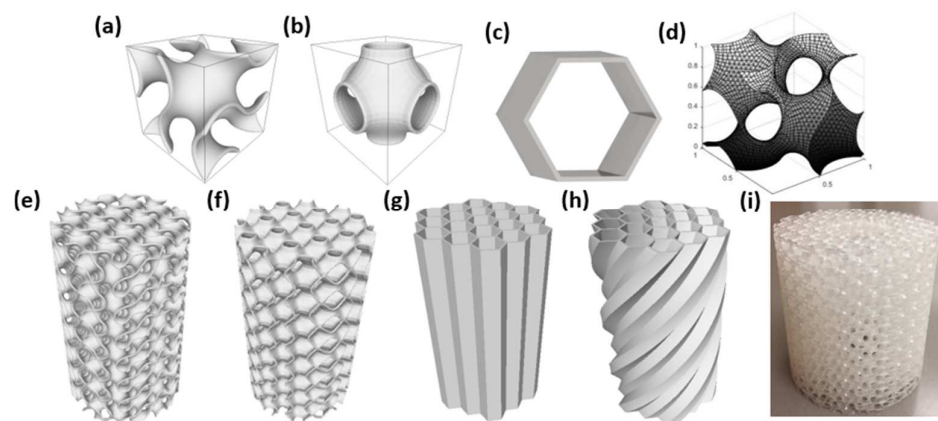


Figure 16. Image of armored grain geometries: (a) gyroid cell; (b) Schwarz P cell; (c) honeycomb cell; (d) Schoen gyroid cell; (e) gyroid structure; (f) Schwarz P structure; (g) straight honeycomb structure; (h) twisted honeycomb structure; (i) Schoen structure. Images adapted from Refs. [44,46] with permission.

In a similar work, Hill et al. [46] tested armored grains that comprised a PLA Schoen gyroid (10 vol.%) embedded in paraffin, as shown in Figure 16i. Ballistic tests from a 2D slab burner showed that the addition of the embedded structure slightly decreased regression rates [46], which contradicts conclusions that can be drawn from the findings at SPLab [41–45]. However, the addition of the structure showed potential to decrease sloughing and increase combustion stability. [46] Hill et al. [47] also tested the effects of infill (5–15 vol.%) with ABS and PLA gyroids using low oxidizer mass fluxes. They found that the infill volume of the lattice had a larger impact on regression rates than the type of plastic used [47]. The results suggested that a lattice volume fraction around 5% may increase regression rates while lattice volume fractions above 5% decreased regression rates [47]. Arnold [26] tested armored grains made from a hexagonal honeycomb structure and found similar conclusions. The armored grains were developed using a paraffin/acrylic mix (~80/20 wt.%) and experienced a decrease in regression rates but an increase in combustion efficiency. The straight-port honeycomb and swept honeycomb increased combustion

efficiencies by 4% and 10%, respectively, compared to the straight-port cast wax [26]. This is believed to be due to the reduction in paraffin slumping which was proven to also hold true at elevated initial fuel grain temperatures [33]. It was also found that larger honeycomb sizes (6 wt.% acrylic) decreased combustion efficiency which suggests that the elevated combustion efficiency is attributed to the printed structure [26].

Lin et al. [48] used AM to develop composite fuel grains composed of multiple blades (aluminum or ABS) in a helical framework and embedded in paraffin, as shown in Figure 17. Uniaxial compression tests were performed to determine their respective Young's modulus and yield stress. Combustion properties were determined by performing lab-scale HRE tests with GOX. The mechanical properties of the aluminum grain were an order of magnitude greater than the pure paraffin and ABS-composite grain while the regression rate increased by 52.5% and 18.0%, respectively [48]. The high thermal conductivity of the structure's blades caused the high regression rates from the aluminum-composite grain [48]. The addition of perforations into the aluminum blades also increased the Young's modulus and combustion efficiency by 51.0% and 14.9%, respectively [48].

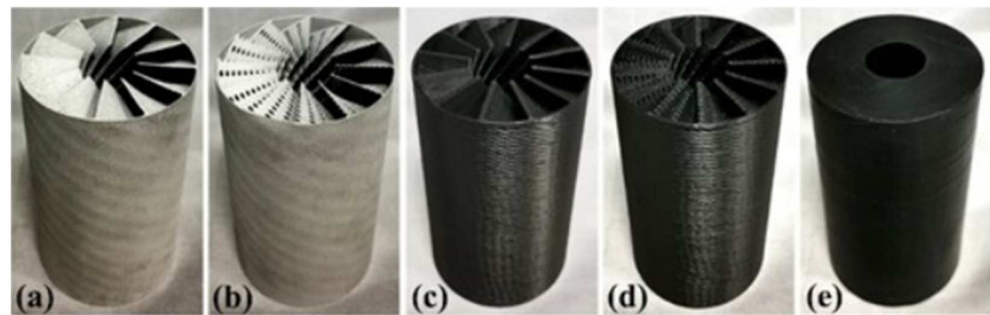


Figure 17. Images of the investigated fuel grain structures: (a) Al blades; (b) Al blades with perforations; (c) ABS blades; (d) ABS blades with perforations; (e) pure paraffin. Image reprinted from Ref. [48] with permission under the Creative Commons 4.0 License.

Wu et al. [49] tested paraffin (58.4 wt.%) fuel grains embedded with a star-shaped skeleton made from seven different materials (ABS, nylon, glass-fiber reinforced nylon, and four other resins) and printed using two techniques (SLA and SLS). Firing tests were conducted using GOX and showed combustion efficiencies around 75–90% [49]. Regression rates were also reported but were not directly compared to any other fuel grains for reference. The ABS-skeleton grain showed the most favorable combustion and mechanical properties [49]. Polymers printed using SLS resulted in greater flame propagation speeds due to rougher prints [49].

Lai et al. [50] designed an armored grain to improve entrainment by using the Kelvin–Helmholtz Instability. The authors tailored the infill of the armored grain based on the supplied oxidizer mass flow rate to amplify the wave-like structures in the liquid layer and promote entrainment [50]. Firing tests with an ABS gyroid structure (28 vol.%) embedded in paraffin showed greater combustion efficiencies than pure paraffin and pure ABS grains [50]. The gyroid grain also outperformed pure paraffin and ABS grains in regression rate, specific impulse, and mean thrust coefficient at high oxidizer mass fluxes (15.3 g/cm²s) but exhibited varied results at lower oxidizer mass fluxes [50].

Meier et al. [51] tested fuel grains infused with gels based on Jet-A fuel. A propylene grain was printed with eight square ports in a concentric pattern that ran axially through the grain, as shown in Figure 18. The square ports were filled with gels containing different additives including fumed silica (5 wt.%), nano-aluminum (5 or 20 wt.%) with fumed silica (4 wt.%), or paraffin (5 or 20 wt.%). Pure propylene grains (baseline) and propylene grains filled with paraffin wax were also developed for comparison purposes. Rheological measurements were performed to characterize the material properties of the gels that affect liquid entrainment. Firing tests were performed on a lab-scale hybrid rocket with GOX as the oxidizer. The paraffin-based gel experienced regression rate increases between

58–84% over the baseline and outperformed its paraffin-filled counterpart [51]. Higher nano-aluminum content led to reduced regression rates despite the increased combustion temperatures due to increased fuel viscosity and decreased fuel entrainment. The performance of the gel-based fuel grains was sensitive to the oxidizer mass flow rate with the best performances experienced at high flow rates. The gel-based fuel grains also substantially decreased O/F ratios compared to traditional fuels. At stoichiometric O/F ratios, the gel-based fuels experienced similar combustion efficiencies to baseline fuels (85–95%) which demonstrated that the gels are completely burned [51]. Mass-based regression methods were also used to determine an effective linear regression rate by assuming a uniformly linear burn due to the unique port geometry.

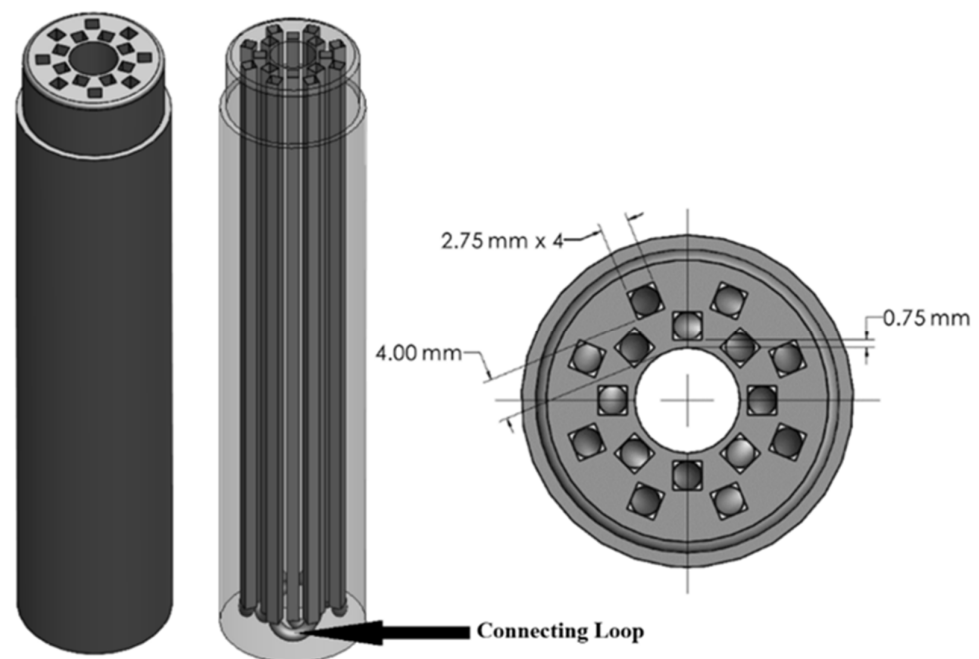


Figure 18. Solid propylene grain with gel-filled ports in a concentric pattern. Image reprinted from Ref. [51] with permission from AIAA.

Oztan et al. [52] used FDM to print ABS fuel grains loaded with paraffin fuel that were incorporated with carbon dots (1 wt.%), as shown in Figure 19. Ballistic tests were performed on a lab-scale HRE with GOX, and the results were compared to an ABS/pure paraffin sample of the same size. The addition of carbon dots showed an increase in regression rates of 11%, an increase in combustion efficiency of 8.5%, and a decrease in compressive strength of 5% [52].

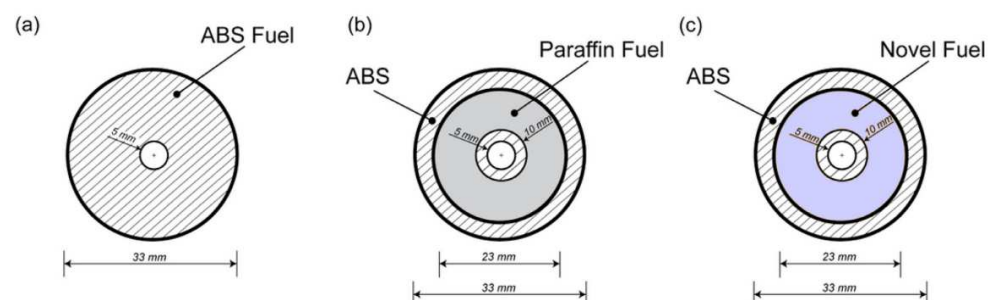


Figure 19. Cross-sectional dimensions of the fuel grains investigated: (a) ABS; (b) ABS and pure paraffin; (c) novel fuel containing carbon dots. Image reprinted from Ref. [52] with permission from Elsevier.

2.3.3. Matrices

Fuel grains have been printed with matrices containing pockets of liquid or powdered fuels to increase regression rates. The fuels stored in the pockets are more energetic and burn faster than solid fuel. As the solid fuel regresses and the pockets open, energetic fuel enters the combustion chamber and increases the combustion temperature while simultaneously increasing the solid fuel surface area, which causes the solid fuel to regress faster and open more pockets. The use of matrices has been shown to be effective at increasing regression rates but can also decrease the combustion efficiency if the stored fuel is not completely burned before being expelled from the combustion chamber.

Fuller and DeSain [53] tested small fuel grains printed in unique geometries filled with liquid kerosene (up to 45 g). Various grain geometries were tested, including stacked cone, spiral, liquid-enhanced hybrid, and canted spiral and tapered wall port, as shown in Figure 20. Chamber pressure, thrust, specific impulse, and regression rates increased with an increasing amount of liquid kerosene [53]. The kerosene-filled fuel grains outperformed solid ABS grains.

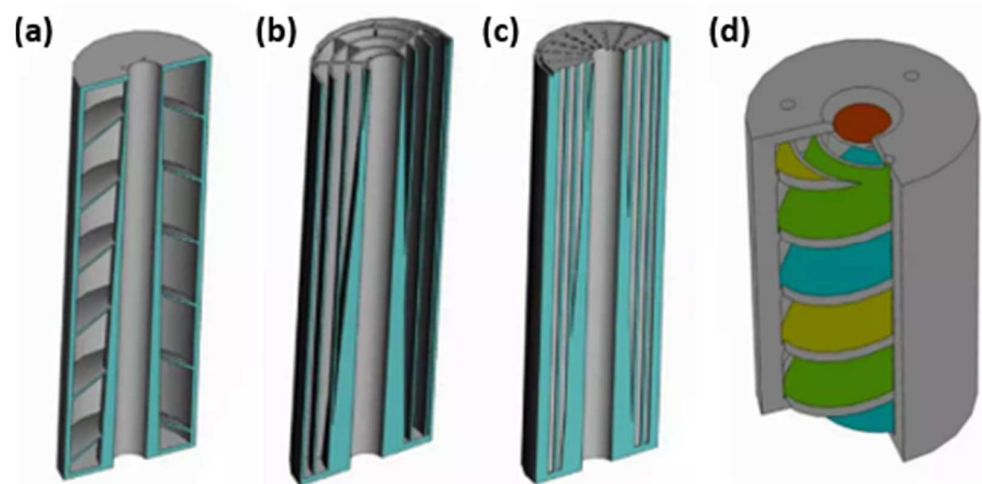


Figure 20. Investigated grain geometries that were filled with kerosene: (a) stacked cone; (b) spiral; (c) liquid-enhanced hybrid; (d) canted spiral and tapered port wall. Image reprinted from Ref. [53] courtesy of and by permission of the Aerospace Corporation.

McCulley [54] tested ABS fuel grains containing “hollow” holes filled with paraffin, as shown in Figure 21. The effects of adding carbon black (1% by mass) and a helical port were also investigated for the constant mixture ratio grains. McCulley observed that both configurations of fuel grains contained similar regression rates that were three times that of pure ABS but had drastically different mass fluxes [54]. The addition of carbon black and the helical port increased combustion efficiencies by 6% and 7% over pure paraffin grains, respectively [54]. However, the paraffin portions burned faster than the ABS portion, which resulted in a significant portion of unused fuel.

Aarant et al. [55] developed fuel grains consisting of an ABS matrix (~50 vol.%) filled with powdered graphite similar to Figure 21a. Tests were performed with varying fuel grain lengths in an effort to obtain the optimal O/F ratio. For intermediate grain lengths, the ABS/graphite grain increased regression rates by 223% and 1.7% over pure ABS and paraffin grains, respectively, but the combustion efficiency decreased by 15.6% and 14.1%, respectively [55]. The authors believe that the increase in fuel regression is due to an increase in surface area from the powdered fuel [55]. The decrease in combustion efficiency can be related to problems regarding the loss of unburned fuels experienced in preliminary tests [56].

Barnhill et al. [57] printed fuel grains containing an ABS matrix filled with anthracite coal. The performance of this grain was compared to fuel grains containing solid ABS and polybutadiene acrylonitrile (PBAN) with 10% aluminum in a matrix configuration. A single

firing test was conducted for each grain on a vertical test stand with nitrous oxide. The coal-packed matrix had a specific impulse of 144.2 s which was a 27.4% and 52.4% increase over the PBAN and ABS grains, respectively [57]. The coal-packed grain also experienced the highest peak and average thrusts. Adding a post-combustion chamber increased the combustion efficiency by 19% which resulted in 86% efficiency [57].

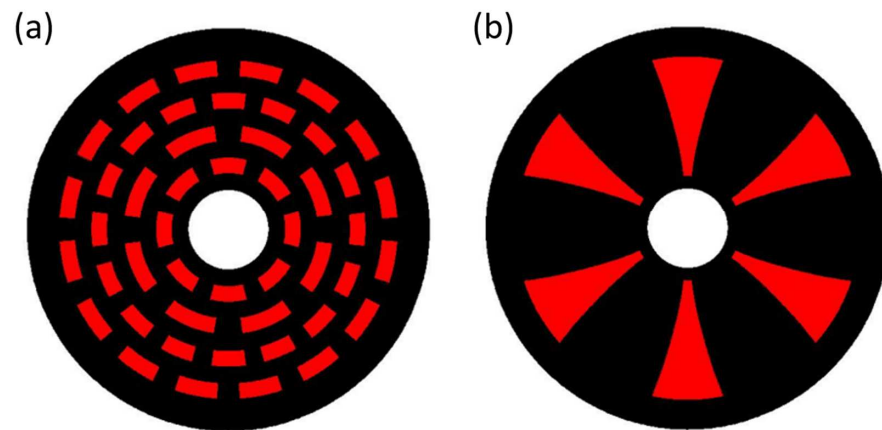


Figure 21. Images of fuel grains investigated by McCulley. Black represents ABS and red represents paraffin: (a) 25% paraffin fuel grain; (b) constant mixture ratio fuel grain. Image reprinted from Ref. [54] with permission.

2.3.4. Flow Modifiers

Diaphragms are discs implemented axially along the port that protrude into the oxidizer stream which creates recirculation zones and enhances mixing to potentially increase the overall combustion efficiency and local regression rate [58]. McKnight et al. [28] printed paraffin fuel grains containing two acrylic diaphragms with thicknesses of 0.050" and 0.100", as shown in Figure 22. Both diaphragms were shown to increase regression rates downstream but also decreased the combustion efficiency. An acrylic mixing section was also added downstream. The regression rate of the paraffin section performed as expected, but the regression rate of the acrylic section was lower than the correlation provided by Doran et al. [59]. However, the combustion efficiency significantly improved and surpassed the straight port paraffin baseline [28].



Figure 22. Comparison of 0.100" diaphragm (left) and 0.050" diaphragm (right). Image reprinted from Ref. [28] courtesy of and by permission of the Aerospace Corporation.

Turbulators are devices embedded into fuel grains to increase regression rates by swirling local combustion gases. Figure 23 shows a triple-vane turbulator insert along with a fuel grain utilizing the turbulator. Arnold [26] investigated fuel grains made from single-vane and triple-vane turbulators filled with paraffin wax in a hexagonal honeycomb structure. The single-vane (ABS) and triple-vane (acrylic) turbulators increased regression rates by 35% and 55%, respectively, compared to similar grains without the turbulators. Only a limited number of tests were conducted, so other definitive conclusions cannot be made.

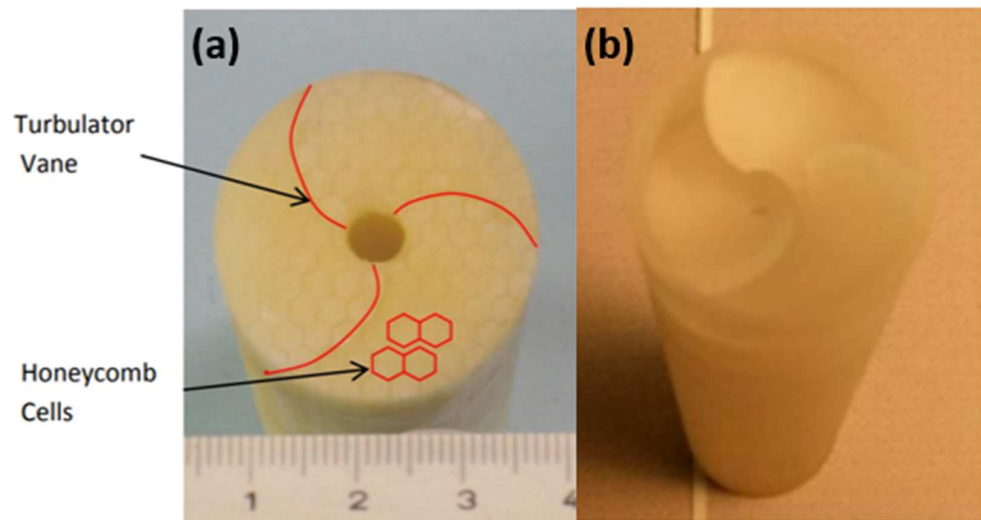


Figure 23. Photographs of turbulator vanes: (a) triple-vane turbulator honeycomb grain; (b) acrylic triple-vane turbulator insert. Image reprinted from Ref. [26] with permission from AIAA.

2.3.5. Metallic Additives

Hybrid rocket fuels commonly incorporate metals due to their high density and energy content. The addition of metals can increase adiabatic flame temperatures, heat of combustion, and radiation heat transfer, resulting in increased regression rates. The metals are homogeneously mixed into the fuel as micro- or nano-scale particles. Nano-scale particles generally outperform micro-scale particles in enhancements towards heat transfer processes and regression rates but are more expensive to manufacture.

Young et al. [29] investigated the effects of aluminum in PMMA grains with a cylindrical and swirl-ellipse port geometry. A custom 3D printer was developed to print grains containing 10 and 25 wt.% nano-aluminum particles (80 nm) and 25 wt.% micro-sized aluminum particles (3.5 μm). Overall, the addition of aluminum particles increased average regression rates but slightly decreased combustion efficiencies. The 25 wt.% nano-aluminum grain with a swirl-ellipse port experienced the greatest regression rates which nearly increased by 150% compared to a solid PMMA [29]. Fuel grains containing the micro-sized aluminum particles had slightly lower regression rates than nano-aluminum grains but also experienced slightly higher combustion efficiencies. The 25 wt.% nano-aluminum grains experienced the greatest chamber pressures which can be due to the higher regression rates or slag accumulation at the nozzle throat, resulting in a decreased diameter [29].

Yenawine [27] tested a single ABS fuel grain containing 3 wt.% aluminum (44 μm) with a star-swirl port geometry, as shown in Figure 24. The ballistic performance of the grain was compared to a similar grain containing pure ABS with a star-swirl port geometry. The addition of the aluminum particles resulted in no notable changes in regression rate and combustion efficiency which may be attributed to their low percentage in the fuel grain, manufacturing flaws, and a limited number of tests [27].

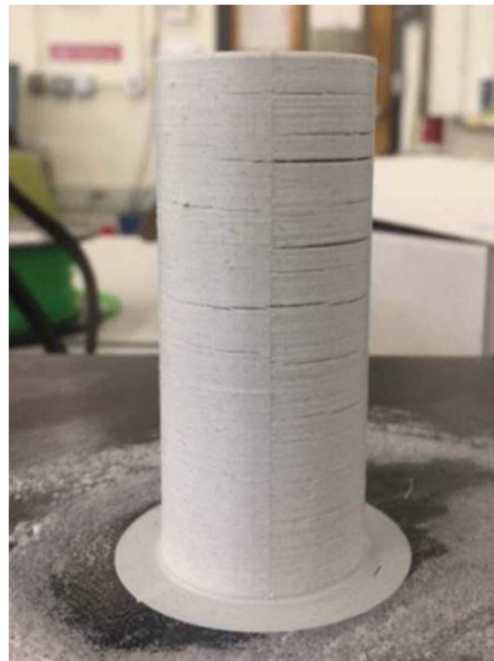


Figure 24. FDM printed ABS + Al fuel grain containing cracks. Image reprinted from Ref. [27] with permission.

Arnold [26] investigated the effects of adding micron-sized aluminum particles (20 wt.%) with paraffin in conjunction with a turbulator and swirl injection. The aluminum particles increased the overall regression rates, increased combustion temperature, and slightly increased the combustion efficiency. In another study, McFarland and Antunes [22] mixed aluminum powder with PLA. However, the addition of aluminum had little effect due to the large particle size which caused the aluminum particles to be ejected from the motor before melting their aluminum oxide coating [22].

Whitmore et al. [60] tested ABS fuel grains with varying levels of 350-mesh copper (2, 4, 6 wt.%). Due to the increase in fuel density and thermal conductivity, the grain exhibited an increase in regression rate, mean thrust levels, and volumetric efficiency with little detrimental effect on the mechanical and chemical efficiency [60]. However, an insufficient number of tests have been performed, so it should be noted that the effects of copper infusion are anecdotal and may not be universal.

2.3.6. Summary

In this section, the effects of an embedded structure, matrices, flow modifiers, and metallic additives were discussed. The embedded structures were generally filled with paraffin or gels and resulted in an increase in regression rates, mechanical properties, and combustion efficiency. The matrices were filled with powdered or liquid fuels and generally resulted in an increase in regression rates but a decrease in combustion efficiency due to the fuel being expelled from the system before completely burning. Two flow modifiers (diaphragms and turbulators) were introduced which both increased regression rates. Nano-aluminum, micro-aluminum, and micro-copper were mixed into thermoplastic AM fuels and resulted in an increase in regression rates and combustion temperature but showed disparate results for combustion efficiency.

2.4. Axial-Injection End-Burning Hybrids

End-burning occurs in cylindrical fuel grains with an array of small ports. Oxidizer flows through each port in the axial direction and creates small diffusion flames at the end. This causes the fuel grain to regress axially instead of radially, as shown in Figure 25. Each diffusion flame at the end of each port expands outwards and eventually merges to create

a steady burn. The regression rate of end-burning hybrid rockets (EBHRs) is characterized by pressure instead of the oxidizer mass flow like traditional HREs. The regression rate of EBHRs is correlated as:

$$\dot{r} = aP_c^n \tag{9}$$

where P_c is the chamber pressure and a and n are empirically fitted constants. End-burning results in a constant burning surface area and elimination of an O/F shift once a steady burn is achieved. However, it is paramount for EBHRs to be manufactured with small, accurate, and consistent port diameters placed across the entire fuel grain’s burning surface to avoid backfiring which causes the flame to instantaneously spread to the upper end of the fuel grain [61]. Saito et al. [62] list the three requirements for a successful axial-injection EBHR as: (1) high initial fuel area fraction for obtaining an optimal O/F, (2) small port intervals for decreasing the time it takes for ports to merge, and (3) ports arrayed across the entire fuel section. True axial-injection EBHRs have only been tested recently with the improvement of AM techniques due to these requirements.

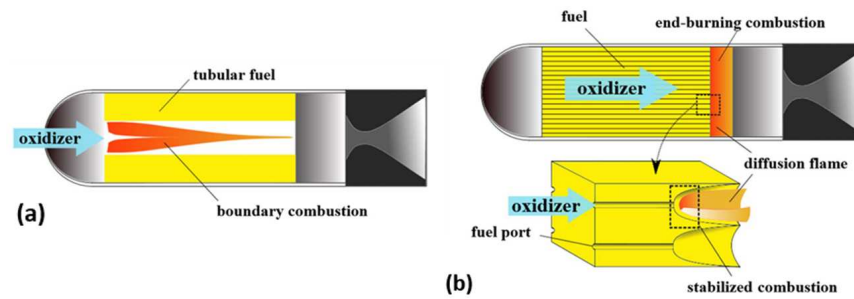


Figure 25. Representation of (a) traditional hybrid rocket and (b) axial-injection end-burning hybrid rocket. Image reprinted from Ref. [62] with permission from AIAA.

The oxidizer port velocity is also important to prevent backfiring, as demonstrated in Figure 26. Backfiring occurs in the flame spread zone when the oxidizer velocity is too low. End-burning occurs in the regression mode when oxidizer flow is sufficient. The fuel grain will enter the blow-off zone when the oxidizer port velocity is too high, preventing flow separation and causing the flames to expand the port diameter, creating a recirculation zone. The Damköhler number (Da) can be used to define the boundary between the flame spread zone and regression mode when using gaseous N_2O and O_2 as oxidizers [63,64].

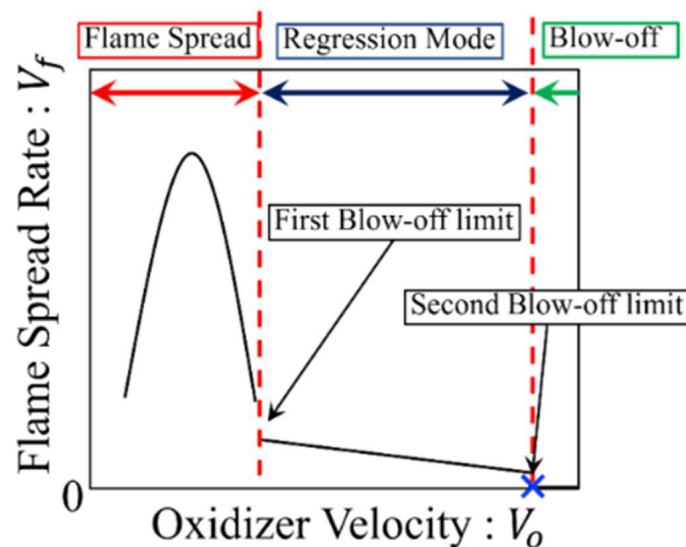


Figure 26. Relationship between combustion mode and oxidizer velocity. Image reprinted from Ref. [64] with permission from AIAA.

Saito et al. [62,65] and Okutani et al. [61] used a high-precision 3D printer to develop an end-burning fuel grain made from 80–90% acrylic acid ester, 5% hexamethylene acrylate, and a photopolymerization initiator, as shown in Figure 27. The fuel grains had a high initial fuel area fraction, small port intervals, and the port arrays spanned the entire fuel surface. Sets of lab scale firing tests were conducted with GOX at pressures ranging from 0.10–0.43 MPa [62], 0.22–1.05 MPa [65], and 0.98–1.44 MPa [61]. The regression rates showed a dependence on chamber pressure with pressures of 0.1, 0.71, and 1.44 MPa, experiencing regression rates of 0.48, 5.38, and 12.6 mm/s, respectively [61,62,65]. Figure 28 also illustrates the relationship between fuel regression rate and chamber pressure for medium-pressure tests. Constant O/F ratios were experienced after a short transient period which confirmed end-burning during the tests [62,65]. For the low-pressure tests, small fuel grains were used and experienced higher regression rates at lower oxidizer port velocities [62]. However, results from medium-pressure tests (larger fuel grains with tighter port intervals) contradict these findings which showed no effects on fuel regression rates from oxidizer flow rates between 31–103 m/s [65]. Switching to the larger fuel grains also showed no scaling effect on regression rates due to its dependence on heat flux from the flame to the fuel surface [65]. High-pressure tests exhibited incredibly high regression rates compared to traditional HREs, but only four tests were performed. Using the same fuel grains, Nagata et al. [66] compared the effects of a tapered port to a straight port. The tapered port reduced transient times from six seconds to less than one second, resulting in end-burning being achieved much faster [66].



Figure 27. Fuel grains made from 80–90% acrylic acid ester, 5% hexamethylene acrylate, and a photopolymerization initiator. Image reprinted from Ref. [62] with permission from AIAA.

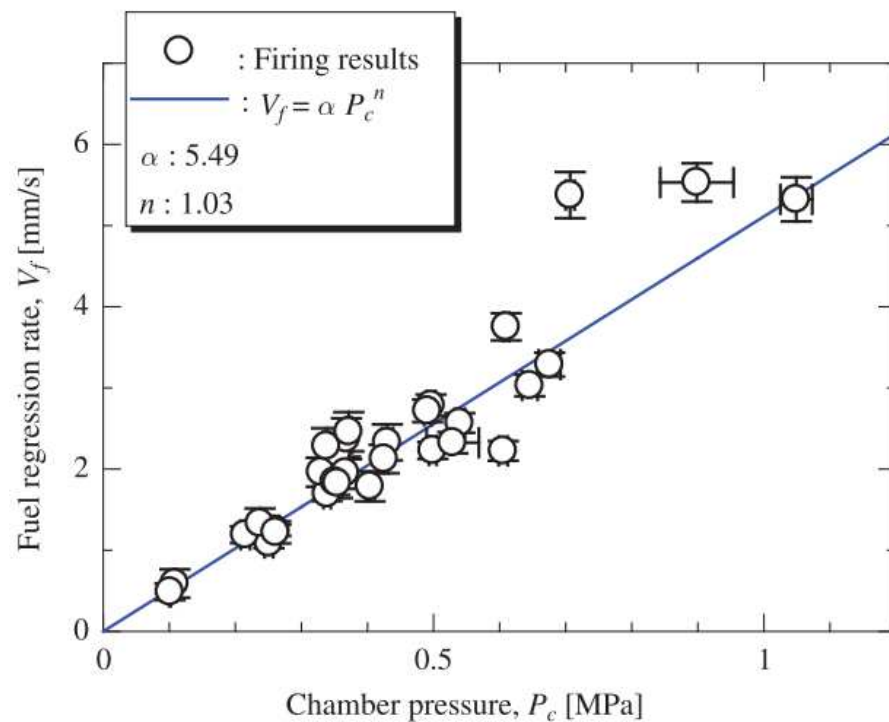


Figure 28. Relationship of regression rate vs. chamber pressure with a single-variable trend line. Image reprinted from Ref. [65] with permission from AIAA.

Okuda et al. [67] burned fuel grains containing 80–90% acrylic acid ester, 5% hexamethylene acrylate, and a photopolymerization initiator with nitrous oxide instead of GOX. A nozzle closure and a melting nozzle were used to increase the initial chamber pressure and promote the formation of stabilized combustion. Twelve tests were performed with one being partially optically accessible. The firing tests with nitrous oxide showed surprisingly high regression rates, which were as high as results from previous tests using GOX. Large fuel flakes (~2 mm) were observed flowing downstream within the combustion gas along with cracks propagating irregularly in the fuel grain. The chamber pressure histories showed no large pressure spikes despite the large flakes of fuel. The authors believe that a new combustion mode exists which is characterized by high regression rates caused by the large flakes of fuel and fast propagation speed of cracks in the fuel grain. Burning the UV-based fuel with nitrous oxide also resulted in a skewed burning surface as opposed to a flat burning surface when fired with GOX, as shown in Figure 29.

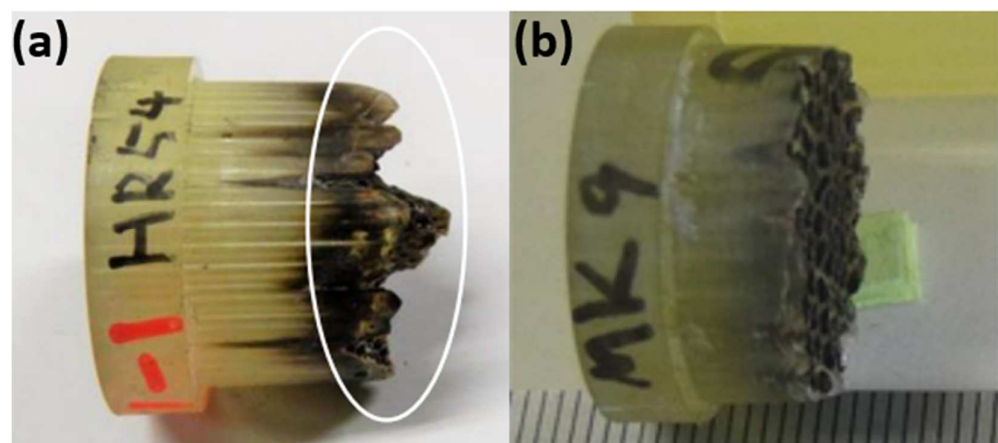


Figure 29. Comparison of UV-based fuel grains burned with different oxidizers: (a) nitrous oxide [67] and (b) GOX [62]. Images reprinted from Refs. [62,67] with permission from AIAA.

Hitt and Agnew [68] investigated the effects of photopolymer material (Somos WaterClear Ultra, Visijet, and Castable Wax), grain size (20, 22, and 53.4 mm diameter), and chamber pressure (168–1780 kPa) on EBHR performance. Multiple lab-scale firings were performed with GOX on the SLA-printed grains. The firings determined the pressure exponent values for Somos WaterClear Ultra, Visijet, and Castable Wax to be 1.5, 1, and 0.6, respectively, with higher exponent values resulting in higher regression rates [68]. The fuel grains made from the chosen materials were also shown to be reliable with multiple firings [68]. The authors noted that future efforts in scaling EBHRs requires accounting for oxidizer port exit areas to ensure proper scaling of the oxidizer velocity which is believed to affect regression rates.

Hitt [69,70] used FDM to print an EBHR fuel grain made from ABS. Fuel grains had port sizes of 0.76 mm [69] and 1.18 mm [70] and were burned with GOX. The fuel grains commonly experienced side-burning and backfiring which is thought to be from insufficient sealing of the grain when using the FDM printing method [69,70]. The author circumvented this problem by applying additional sleeves around the grain. Figure 30 shows fuel grains pre- and post-test, side-burning, and the additional sleeve applied. The firing tests showed that regression rates were influenced by the chamber pressure and the distribution of oxidizer ports with higher regression rates experienced near the oxidizer ports [69].

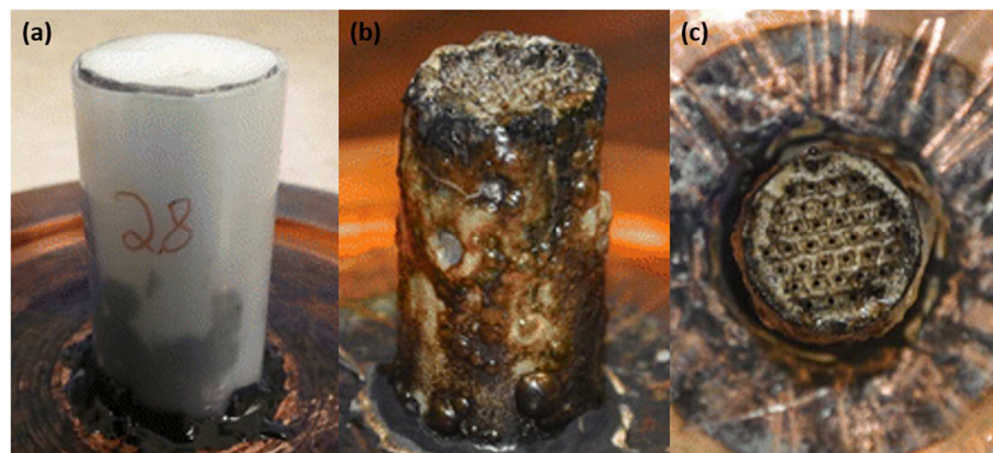


Figure 30. FDM-printed fuel grain used for end-burning tests: (a) pre-test ABS grain; (b) post-test grain with side-burning; (c) post-test grain with additional sleeve. Image reprinted from Ref. [70] with permission from AIAA.

Hirai et al. [71] achieved end-burning using the FDM printing method with PLA resin. Firing tests between 10–50 s were performed without experiencing any side-burning or backfiring. The fuel grain also experienced a relatively constant O/F ratio after a 15–20 s transient period which confirmed end-burning. Microscopic port holes were developed by using the FDM printer’s uniform stacking function and changing the internal fill structure. The printed layers are uniformly stacked in a neat pattern when using a low infill percentage. However, this pattern can be changed so the void space is stacked vertically and creates ports for oxidizer flow. The stacked void spaces become small enough for end-burning to be achieved at infill percentages above 95% [71].

More fuel materials can be explored with EBHRs now that FDM printing of these systems has been successfully demonstrated. UV-based fuels were used due to the material limitations of SLA methods and their capabilities of producing high-accuracy prints needed to achieve end-burning. EBHRs can now be explored with different materials such as ABS, PLA, and PMMA or with metallic additives. EBHRs will become more popular with the new printing materials, constant O/F ratio, scalability, ease of manufacturing, and high volumetric loading efficiency.

2.5. Literature Review Summary

The experimental effects of additive manufacturing on hybrid rocket fuels are explored through fuel systems containing complex combustion port geometries, multiple fuels, and end-burning. Complex combustion port geometries include helical and swirling ports with cylindrical, ellipse, and star shapes which are not feasible to manufacture with subtractive or casting methods. Multi-fuel systems include complex structures embedded in fuel which can only be produced using additive techniques. The end-burning phenomenon is only possible with high precision AM to produce port arrays that are sufficiently small and consistent. A large variety of fuels are printable with varying characteristics, but the most common fuels include ABS, PLA, Nylon 6, and paraffin- and UV-based fuels. These fuels have generally been compared to each other or HTPB, which was demonstrated to perform similarly to ABS by Whitmore et al. [17].

The effects of a helical and swirling port along with cylindrical, ellipse, and star shapes on fuel performance were documented in the Complex Combustion Port Geometries section. The performance of fuel grains containing helical ports were significantly affected by pitch length with regression rates increasing from the application of smaller pitch lengths. Helical ports cause a centrifugal flow pattern which enhances the surface skin friction, thins the wall boundary layer, decreases the blowing effect, and increases the convective heat transfer to the burning surface. The performance of fuel grains containing swirling ports were significantly affected by their turns-per-inch with regression rates increasing with a higher number of turns-per-inch. The swirling port causes a swirling motion of the oxidizer flow which increases the turbulence and mixing of the oxidizer with the fuel. The effect of helical and swirling ports on combustion efficiencies showed disparate results. The effects on fuel performance from these unique port geometries diminish with burn-time as the combustion port becomes more cylindrical and straight.

Embedded structures, matrices, flow modifiers, and metallic additives were discussed in the Multi-Fuel Printed Systems section. A variety of fuels have been explored, including thermoplastics, metals, liquid fuels, powdered fuels, and liquifying fuels. Filling the embedded structures with paraffin or gels generally caused increases in regression rates, mechanical properties, and combustion efficiency. Powdered or liquid fuels were embedded in the matrices which resulted in an increase in regression rates but a decrease in combustion efficiency due to the fuel being expelled from the system before it was completely burned. Diaphragms and turbulators were introduced as AM flow modifiers and both increased regression rates. Mixing nano-aluminum, micro-aluminum, and micro-copper into the AM fuels resulted in increased regression rates and combustion temperatures, but disparate results for combustion efficiency were reported.

In the End-Burning section, it was demonstrated that the fuel regression rate of EBHRs was dependent on chamber pressure and oxidizer velocity instead of oxidizer mass flux. Fuel regression rates increased as the chamber pressure increased. End-burning was achieved from SLA printing with UV-based fuels and is characterized by axial fuel regression with a constant O/F ratio after a short transient period. End-burning tests were performed with both GOX and nitrous oxide as the oxidizers but experienced different burning properties. Common problems experienced include backfiring and side-burning due to improper oxidizer velocity or insufficient sealing while printing with the FDM method. However, Hirai et al. [71] were recently able to achieve end-burning using an FDM printer with PLA fuel.

3. Theoretical Performance Analysis

Chemical equilibrium analysis can be utilized to evaluate the theoretical performance of fuel and oxidizer combinations based on the relative concentrations of their constituent chemicals and their corresponding thermochemical properties [72,73]. CEA calculations are utilized here to evaluate the potential differences in theoretical performance of additively manufactured (AM) fuels that could be used for hybrid rocket applications. A set of fuels including ABS, PLA, PMMA, PC, Nylon 6, and a representative UV-curable fuel are

considered alongside HTPB as a baseline. The two most common hybrid rocket oxidizers, LOX and N_2O , are considered. In the following sub-section, the properties of these fuels and oxidizers are sourced from the literature and estimated by theoretical methods. These properties are subsequently used in CEA computations to predict the theoretical ballistic performance and to make comparisons between the fuels.

3.1. Fuel and Oxidizer Property Estimations

The chemical formula, heat of formation, and density of all chemicals are required to perform CEA calculations. The density and heat of formation for all the fuels considered here were sourced from the literature [17,67,74–78]. However, the methods presented in the literature to estimate or measure the heats of formation of the fuels varied drastically. The group additive calculation procedure presented by Walters, Hackett, and Lyon [79–82] was therefore used to estimate the heats of formation of all the fuels and to provide a consistent basis for comparison. In particular, the heats of formation of the polymeric fuels were computed from the definition of the stoichiometric heat of combustion which was directly estimated from a group additive method [80]. The one exception was for the representative UV-curable fuel which could not be computed due to a lack of information regarding its composition, so an experimental value provided by Okuda et al. [67] was implemented instead. The density values provided in the literature were consistent and were therefore retained here. All fuel properties are presented in Table 2. Relatively good agreement is observed between the heats of formation taken from the literature and those predicted by the group additive method here which validates the approach for estimation of this property for the AM fuels.

Table 2. Predicted and literature properties for common AM plastic fuels found in the hybrid rocket literature.

Fuel Name	Fuel Formula	Molecular Weight (g/mol)	Density (kg/m ³)	Theoretical		Heat of Formation		Reference
				(kJ/mol)	(kJ/kg)	(kJ/mol)	(kJ/kg)	
Hydroxyl-Terminated Polybutadiene (HTPB)	(C ₄ H ₆) _n	54	930	209	3867	342	6321	Thomas and Petersen, 2022 [74]
Acrylonitrile Butadiene Styrene (ABS) (43/50/7)	(C _{3.85} H _{4.85} N _{0.43}) _n	57	975	198	3463	63	1096	Whitmore et al., 2013 [17]
Poly(lactic acid) (PLA)	(C ₃ H ₄ O ₂) _n	72	1240	−259	−3595	−302	−4194	Ahn et al., 2021 [75]
Poly(Methyl Methacrylate) (PMMA)	(C ₅ H ₈ O ₂) _n	100	1180	−172	−1715	−622	−6212	Zeng et al., 2002 [76]
Polycarbonate (PC)	(C ₁₆ H ₁₄ O ₃) _n	254	1200	27	108	−103	−406	Joshi and Zwolinski, 1968 [77]
Nylon 6	(C ₆ H ₁₁ ON) _n	113	1084	−5	−43	−272	−13	Herps, 2020 [78]
UV-Curable Fuel ^a	(C _{16.09} H _{20.61} O _{3.97}) _n	277	1191	-	-	−297	−1070	Okuda et al., 2022 [67]

^a 80–90% acrylic acid ester, 5% hexamethylene acrylate, photopolymerization initiator.

The properties for cryogenic LOX were taken at its boiling point ($T_b = 90$ K) at standard atmospheric pressure, as given by Sutton and Biblarz [12]. The density and heat of formation for LOX prescribed here are 1149 kg/m³ and −13 kJ/mol (−405 kJ/kg), respectively. The properties for storable N_2O were taken for a liquid stored above its vapor pressure at standard temperature, as given by Hesiter and Wernimont [83]. The density and heat of formation for N_2O prescribed here are 1980 kg/m³ and 82 kJ/mol (1854 kJ/kg), respectively.

3.2. Chemical Equilibrium Analysis Computations

Chemical equilibrium computations were completed in Praqsys's Cequel program, which is based on NASA's CEA [72,73], for hybrid rocket propellants undergoing combustion at a chamber pressure of 6.89 MPa (1000 psia). The combustion gas properties (specific heat ratio, molecular weight, and adiabatic flame temperature) and rocket performance parameters (characteristic velocity, specific impulse, and density specific impulse) were computed for all fuel/oxidizer combinations and over a range of O/F ratios. Rocket performance parameters were computed by assuming perfect nozzle expansion at sea level ($P_e = P_a = 0.101325$ MPa) with shifting chemistry.

The characteristic velocity (c^*) is a thermodynamic property of a specific propellant combination and the combustion chamber conditions (e.g., chamber pressure, P_c). Characteristic velocity is a function of the combustion product temperature (T_{AF}), specific heat ratio (γ), and molecular weight and can be written as a function of the specific impulse (I_{sp}) and thrust coefficient (C_F): $I_{sp} = c^* C_F / g_0$. The thrust coefficient (C_F) is a function of the combustion gas properties, rocket design parameters (e.g., nozzle contraction ratio, $\varepsilon = A_e / A_t$), and combustion conditions (P_c). The specific impulse of a propellant combination is defined as the total impulse delivered per unit mass of propellant or, equivalently, the thrust force generated per unit of propellant mass flow rate ($I_{sp} = F / \dot{m}_p g_0$). The density specific impulse is similarly defined as the total impulse delivered per unit volume of propellant ($I_{sp,v} = \rho I_{sp}$) but is normalized here by the specific gravity of the propellant combination: $I_{sp,v} = (\rho / \rho_{H_2O}) I_{sp}$. In general, optimizing specific and density specific impulse is relevant for mass- and volume-limited systems, respectively. Hybrid rockets generally fall into the volume-limited category so that density specific impulse is a more relevant performance parameter, but this is not universally true.

3.2.1. Baseline Fuels

CEA computations were completed for all fuels listed in Table 2, reacting with LOX or N₂O. The predicted adiabatic flame temperature, specific impulse, and density specific impulse for all fuel/oxidizer combinations are presented in Figure 31. In addition, the maximum theoretical performance parameters for each fuel/oxidizer combination are provided in Table 3 for comparison. The theoretical specific and density specific impulse values are relatively closely grouped amongst the different potential fuels. For example, the range of theoretical specific and density specific impulse values for all fuels reacting with LOX lies within 262–300 and 313–324 s, respectively. None of the potential AM fuels outperform HTPB's maximum specific impulse for either oxidizer but several are comparable, and ABS is the best AM alternative for this performance metric. In contrast, the density specific impulse of several of the AM fuels (PMMA, PC, Nylon 6, and UV Fuel) reacting with LOX are greater than that of HTPB. However, none of the AM fuels exhibit a density specific impulse greater than HTPB when N₂O is used as the oxidizer. Furthermore, PLA exhibits the lowest theoretical performance for both oxidizer cases. It is also interesting to note that the UV-curable fuel exhibits a very similar theoretical performance to the thermoplastic polymers. In all cases, utilization of an AM fuel instead of HTPB shifts the peak operating condition to lower O/F ratios. This is a positive design aspect because it translates to optimized performance with smaller oxidizer tanks and corresponding inert vehicle mass.

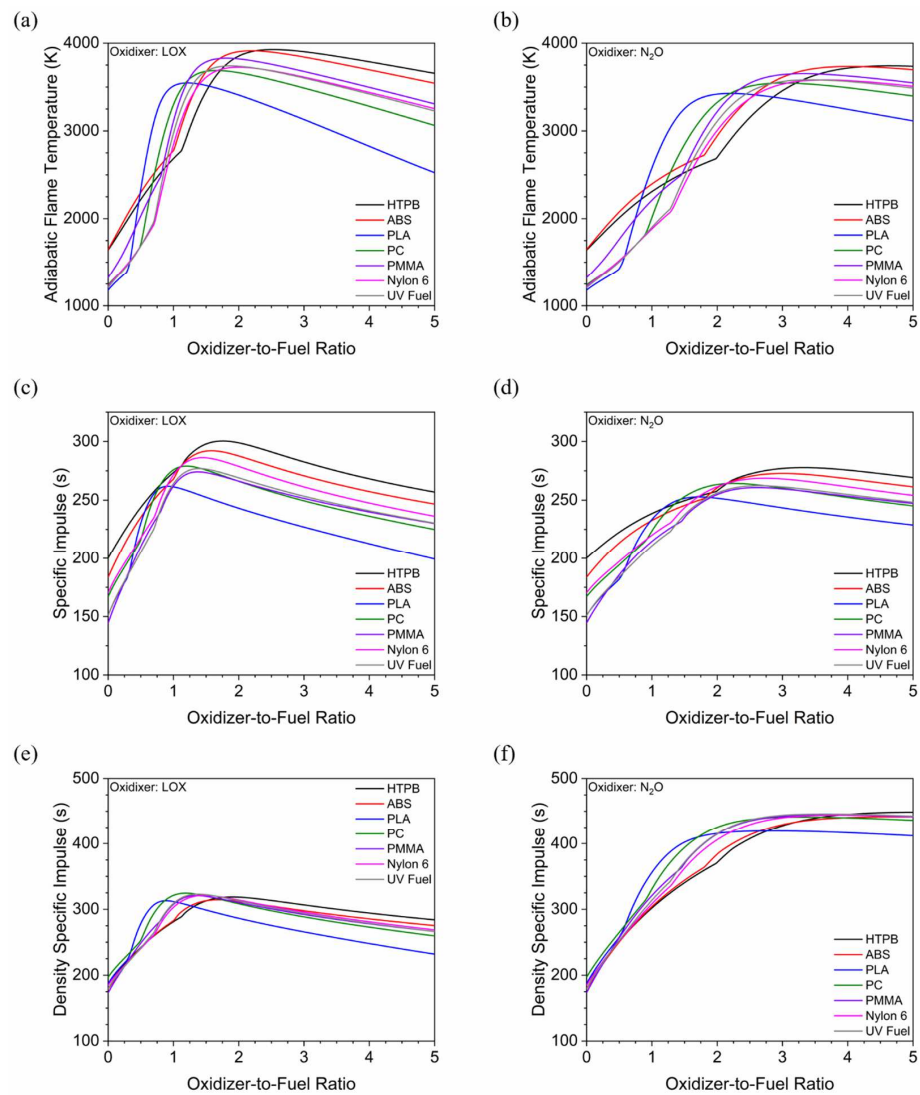


Figure 31. Theoretical ballistic performance of hybrid rocket propellants reacting at 6.89 MPa (1000 psia): (a,b) adiabatic flame temperature; (c,d) specific impulse; (e,f) density specific impulse of HTPB and potential AM fuels reacting with (left) LOX and (right) N₂O.

Table 3. Compilation of maximum theoretical performance of HTPB and potential AM fuels reacting with LOX or N₂O.

Fuel	Oxidizer	Maximum Theoretical Performance Parameter			
		T_{AF} (K)	c^* (m/s)	I_{sp} (s)	$I_{sp,v}$ (s)
HTPB	LOX	3927	1874	300	319
ABS	LOX	3913	1822	292	314
PLA	LOX	3547	1611	262	313
PMMA	LOX	3689	1724	279	324
PC	LOX	3829	1702	274	321
Nylon 6	LOX	3726	1773	286	321
UV Fuel	LOX	3741	1715	277	323
HTPB	N ₂ O	3742	1737	278	449
ABS	N ₂ O	3735	1706	273	442
PLA	N ₂ O	3427	1564	253	419
PMMA	N ₂ O	3546	1642	264	441
PC	N ₂ O	3653	1626	261	444
Nylon 6	N ₂ O	3581	1672	269	444
UV Fuel	N ₂ O	3582	1632	262	446

3.2.2. Inclusion of Metallic Additives

The effects of including metallic additives in an AM fuel are demonstrated in Figure 32, which shows the theoretical performance of aluminum-loaded ABS reacting with LOX. The addition of aluminum increases the adiabatic flame temperature, decreases the specific impulse, increases the density specific impulse, and shifts the peak performance O/F ratio to lower values. The inclusion of 25 and 50% aluminum yields, respectively, increases in density specific impulse of 3.5% (11 s) and 7% (22 s) over the baseline ABS fuel reacting with LOX. The increase in density specific impulse and shift in the optimum O/F ratio to lower values are both positive design aspects for hybrid rocket systems. Similar results are observed for the ABS/N₂O propellant combination and similar metallized fuel systems.

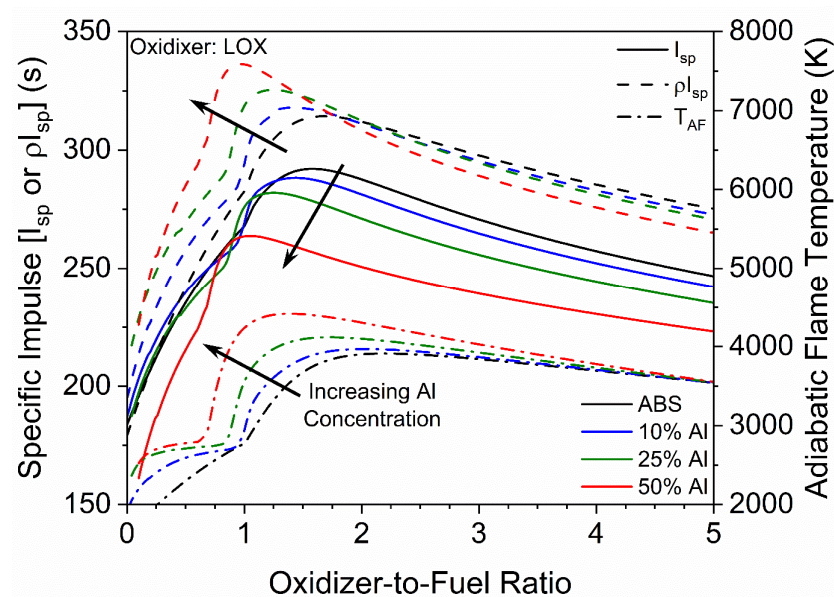


Figure 32. Theoretical ballistic performance of plain and aluminum-loaded ABS reacting with LOX at 6.89 MPa (1000 psia).

3.3. Summary

The CEA computations presented here illustrate how the selection of AM fuel type can influence the theoretical ballistic performance of hybrid rocket systems. Several of the AM fuels evaluated exhibited a theoretical performance similar to the standard hybrid rocket fuel (HTPB). HTPB exhibits the highest theoretical specific impulse, but many of the AM fuels exhibited a greater density specific impulse, which is generally a more relevant parameter for volume-limited propulsion systems, such as hybrid rockets. Replacement of HTPB with any of the AM fuels also shifted the O/F ratio corresponding to maximum performance to lower values. This shift translates to smaller oxidizer tanks and lower inert mass for the design of a propulsion vehicle. Furthermore, the addition of aluminum to an AM fuel (demonstrated with ABS here) yields an increase in the density specific impulse and a similar shift in the O/F ratio corresponding to maximum performance to lower values. These findings indicate that the theoretical performance of AM hybrid rockets can be tailored and optimized by proper fuel design and selection.

4. Conclusions

The performance of HREs is dependent on fuel/oxidizer selection and fuel grain geometry. Novel methods utilizing additive manufacturing to alter the fuel grain geometry have been extensively explored in the literature and were reviewed here. The addition of metallic particles, diaphragms, and turbulators or the use of alternative fuels such as gels, powdered, liquid, and liquifying fuels have been demonstrated to increase fuel regression rates. Helical ports with short pitch lengths or swirling ports with a high number

of turns-per-inch demonstrated the greatest increases in fuel regression rates, but these effects diminished with increasing burn-time. Embedded structures have been shown to improve the yield stress, yield strain, and ductility of the fuel grains while slightly increasing regression rates and combustion efficiencies. End-burning HREs resulted in burns containing a constant O/F ratio with regression rates that are highly dependent on chamber pressure and oxidizer velocity.

CEA computations completed here demonstrated the theoretical performance of AM fuels with varying oxidizers (LOX and N₂O). HTPB showed the greatest maximum specific impulse with both oxidizers, but ABS was comparable and represented the best AM fuel for this performance metric. Many of the AM fuels exhibited greater density specific impulse than HTPB and experienced a shift of the optimal O/F ratio to lower values. The addition of aluminum to ABS followed a similar trend of increasing the density specific impulse and decreasing the optimal O/F ratio.

The application of AM techniques for the design of fuel systems in hybrid rockets is a rapidly evolving technical field with a high degree of novelty. The research in this area over the last two decades has significantly expanded the design space for HREs and has the potential to lead to the application of HREs to propulsion missions where they were previously unable to compete with pure liquid or solid systems. In particular, the ease of manufacturing of FDM systems, the comparable or improved ballistic properties and performance of many readily available AM fuels, and the high degree of design adaptability make AM-fueled HREs competitive for future propulsion systems.

Author Contributions: Conceptualization, C.N. and J.C.T.; methodology, C.N. and J.C.T.; data curation, C.N.; writing—original draft preparation, C.N.; writing—review and editing, C.N. and J.C.T.; supervision, J.C.T. All authors have read and agreed to the published version of the manuscript.

Funding: This research received no external funding.

Data Availability Statement: Not applicable.

Conflicts of Interest: The authors declare no conflict of interest.

References

1. Kuo, K.; Chiaverini, M. *Fundamentals of Hybrid Rocket Combustion and Propulsion*; American Institute of Aeronautics and Astronautics, Inc.: Reston, VA, USA, 2007; Volume 218.
2. Kamps, L.; Hirai, S.; Nagata, H. Hybrid Rockets as Post-Boost Stages and Kick Motors. *Aerospace* **2021**, *8*, 253. [[CrossRef](#)]
3. Oztan, C.; Coverstone, V. Utilization of additive manufacturing in hybrid rocket technology: A review. *Acta Astronaut.* **2021**, *180*, 130–140. [[CrossRef](#)]
4. Bhuvanesh, K.M.; Sathiya, P. Methods and materials for additive manufacturing: A critical review on advancements and challenges. *Thin-Walled Struct.* **2021**, *159*, 107228. [[CrossRef](#)]
5. Ngo, T.D.; Kashani, A.; Imbalzano, G.; Nguyen, K.T.Q.; David, H. Additive manufacturing (3D printing): A review of materials, methods, applications, and challenges. *Compos. B Eng.* **2018**, *143*, 172–196. [[CrossRef](#)]
6. Mohamed, O.A.; Masood, S.H.; Bhowmik, J.L. Optimization of fused deposition modeling process parameters: A review of current research and future prospects. *Adv. Manuf.* **2015**, *3*, 42–53. [[CrossRef](#)]
7. Sood, A.K.; Odhar, R.K.; Mahapatra, S.S. Parametric appraisal of mechanical property of fused deposition modelling processed parts. *Mater. Des.* **2010**, *31*, 287–295. [[CrossRef](#)]
8. Parandoush, P.; Lin, D. A review on additive manufacturing of polymer-fiber composites. *Compos. Struct.* **2017**, *182*, 36–53. [[CrossRef](#)]
9. Wang, X.; Jiang, M.; Zhou, Z.; Gou, J.; Hui, D. 3D printing of polymer matrix composites: A review and prospective. *Compos. B Eng.* **2017**, *110*, 442–458. [[CrossRef](#)]
10. Glaser, C.; Hijckema, J.; Anthoine, J. Evaluation of Regression Rate Enhancing Concepts and Techniques for Hybrid Rocket Engines. *Aerotec. Missili Spaz.* **2022**, *101*, 267–292. [[CrossRef](#)]
11. Marxman, G.A.; Wooldridge, C.E. *Fundamentals of Hybrid Boundary-Layer Combustion*. *Heterog. Combust.* **1964**, *15*, 485–522.
12. Sutton, G.; Biblarz, O. *Rocket Propulsion Elements*, 8th ed.; John Wiley & Sons, Inc.: Hoboken, NJ, USA, 2010.
13. Chiaverini, M. Review of solid-fuel regression rate behavior in classical and nonclassical hybrid rocket motors. In *Fundamentals of Hybrid Rocket Combustion and Propulsion*; Kuo, K., Ed.; American Institute of Aeronautics and Astronautics, Inc.: Reston, VA, USA, 2007; Volume 218, pp. 37–126.
14. Ozawa, K.; Han-wei, W.; Yoshino, T.; Tsuboi, N. Time-resolved fuel regression measurement function of a hybrid rocket solid fuel integrated by multi-material additive manufacturing. *Acta Astronaut.* **2021**, *187*, 89–100. [[CrossRef](#)]

15. Thomas, J.C.; Petersen, E.L.; DeSain, J.D.; Brady, B.B. Enhancement of Regression Rates in Hybrid Rockets with HTPB Fuel Grains by Metallic Additives. In Proceedings of the AIAA Propulsion and Energy 2015 Forum, Orlando, FL, USA, 27–29 July 2015.
16. DeLuca, L.; Galfetti, L.; Maggi, F.; Colombo, G.; Paravan, C.; Reina, A.; Tadini, P.; Sossi, A.; Duranti, E. Time-Resolved Burning of Solid Fuels for Hybrid Rocket Propulsion. *Prog. Propul. Phys.* **2011**, *2*, 341–362.
17. Whitmore, S.A.; Peterson, Z.W.; Eilers, S.D. Comparing Hydroxyl Terminated Polybutadiene and Acrylonitrile Butadiene Styrene as Hybrid Rocket Fuels. *J. Propuls. Power* **2013**, *29*, 582–592. [[CrossRef](#)]
18. Grefen, B.; Becker, J.; Linke, S.; Stoll, E. Design, Production and Evaluation of 3D-Printed Mold Geometries for a Hybrid Rocket Engine. *Aerospace* **2021**, *8*, 220. [[CrossRef](#)]
19. Walker, S.D. High Regression Rate Hybrid Rocket Fuel Grains with Helical Port Structures. Master's Thesis, Utah State University, Logan, UT, USA, 2015.
20. Whitmore, S.A.; Merkley, S.L.; Tunc, L.; Mathias, S.D. Survey of Selected Additively Manufactured Propellants for Arc Ignition of Hybrid Rockets. *J. Propuls. Power* **2016**, *32*, 1494–1504. [[CrossRef](#)]
21. Yu, X.; Yu, H.; Zhang, W.; DeLuca, L.; Shen, R. Effect of Penetrative Combustion on Regression Rate of 3D Printed Hybrid Rocket Fuel. *Aerospace* **2022**, *9*, 696. [[CrossRef](#)]
22. McFarland, M.; Antunes, E. Small-Scale Static Fire Tests of 3D Printing Hybrid Rocket Fuel Grains Produced from Different Materials. *Aerospace* **2019**, *6*, 81. [[CrossRef](#)]
23. Wang, Z.; Lin, X.; Li, F.; Yu, X. Combustion performance of a novel hybrid rocket fuel grain with a nested helical structure. *Aerosp. Sci. Technol.* **2020**, *97*, 105613. [[CrossRef](#)]
24. Zdybal, D.; Pabarcus, L.; Laczewski, A.; Wyciszkiwicz, B.; Zwolak, A.; Slawewski, P.; Wyzlinski, M. Investigation of FDM-printed open-framework-reinforced helical PEWAX grains as a robust, high regression hybrid rocket fuel. In Proceedings of the AIAA Scitech 2021 Forum, Virtual Event, 11–21 January 2021.
25. Tian, H.; Li, Y.; Li, C.; Sun, X. Regression rate characteristics of hybrid rocket motor with helical grain. *Aerosp. Sci. Technol.* **2017**, *68*, 90–103. [[CrossRef](#)]
26. Arnold, D.M. Formulation and Characterization of Paraffin-Based Solid Fuels Containing Swirl Inducing Grain Geometry and/or Energetic Additives. Master's Thesis, The Pennsylvania State University, State College, PA, USA, 2014.
27. Yenawine, A.W. Hybrid Rocket Engines: Development of Composite Fuels with Complex 3D Printed Ports. Master's Thesis, University of Miami, Miami, FL, USA, 2019.
28. McKnight, B.R.; Boyer, E.J.; Nardozzo, P.K.; Cortopassi, A. Design and Testing of an Additively Manufactured Advanced Hybrid Rocket Motor Propulsion Unit for CubeSats (PUC). In Proceedings of the 51st AIAA/SAE/ASEE Joint Propulsion Conference, Orlando, FL, USA, 27–29 July 2015.
29. Young, G.; Connell, T.L., Jr.; Fennell, K.; Possehl, S.; Baier, M. Examining Port Geometry/Solid Loading for Additively Manufactured Fuels in Hybrid Rockets. *J. Propuls. Power* **2021**, *37*, 305–313. [[CrossRef](#)]
30. Connell, T.L., Jr.; Young, G.; Beckett, K.; Gumm, C.; Gonzalez, D.; Baier, M. Enhanced Solid Fuel Regression in a Hybrid Rocket Employing Additively Manufactured Fuels Exhibiting Novel Fuel Grain Port Geometries. In Proceedings of the AIAA Scitech 2019 Forum, San Diego, CA, USA, 7–11 January 2019.
31. Karabeyoglu, M.A.; Altman, D.; Cantwell, B.J. Combustion of Liquefying Hybrid Propellants: Part 1, General Theory. *J. Propuls. Power* **2002**, *18*, 610–620. [[CrossRef](#)]
32. Karabeyoglu, A.; Zilliac, G.; Cantwell, B.J.; DeZilwa, S.; Castellucci, P. Scale-Up Tests of High Regression Rate Paraffin-Based Hybrid Rocket Fuels. *J. Propuls. Power* **2004**, *20*, 1037–1045. [[CrossRef](#)]
33. Arnold, D.M.; Boyer, E.J.; McKnight, B.; Kuo, K.; Desain, J.; Brady, B.B.; Fuller, J.; Curtiss, T.J. Testing of Hybrid Rocket Fuel Grains at Elevated Temperatures with Swirl Patterns Fabricated Using Rapid Prototyping Technology. In Proceedings of the 50th AIAA/ASME/SAE/ASEE Joint Propulsion Conference, Cleveland, OH, USA, 28–30 July 2014.
34. Mengu, D.; Kumar, R. Development of EVA-SEBS based wax fuel for hybrid rocket applications. *Acta. Astronaut.* **2018**, *152*, 325–334. [[CrossRef](#)]
35. Veale, K.; Adali, S.; Pitot, J.; Brooks, M. A review of the performance and structural considerations of paraffin wax hybrid rocket fuels with additives. *Acta. Astronaut.* **2017**, *141*, 196–208. [[CrossRef](#)]
36. Nakagawa, I.; Hikone, S. Study on the Regression Rate of Paraffin-Based Hybrid Rocket Fuels. *J. Propuls. Power* **2011**, *27*, 1276–1279. [[CrossRef](#)]
37. Ishigaki, T.; Nakagawa, I. Improving Physical Properties of Wax-Based Fuels and Its Effect on Regression Rate. *J. Propuls. Power* **2020**, *36*, 123–128. [[CrossRef](#)]
38. Tang, Y.; Chen, S.; Zhang, W.; Shen, R.; DeLuca, L.T.; Ye, Y. Mechanical Modifications of Paraffin-based Fuels and the Effects on Combustion Performance. *Propellants Explos. Pyrotech.* **2017**, *42*, 1268–1277. [[CrossRef](#)]
39. Kumar, R.; Ramakrishna, P.A. Studies on EVA-Based Wax Fuel for Launch Vehicle Applications. *Propellants Explos. Pyrotech.* **2016**, *41*, 295–303. [[CrossRef](#)]
40. Galfetti, L.; Merotto, L.; Boiocchi, M.; Maggi, F.; DeLuca, L. Ballistic and rheological characterization of paraffin-based fuels for hybrid rocket propulsion. In Proceedings of the 47th AIAA/ASME/SAE/ASEE Joint Propulsion Conference & Exhibit, San Diego, CA, USA, 31 July–3 August 2011.

41. Bisin, R.; Paravan, C.; Verga, A.; Galfetti, L. An Innovative Strategy for Paraffin-based Fuels Reinforcement: Part II, Ballistic Characterization. In Proceedings of the 8th European Conference for Aeronautics and Aerospace Sciences (EUCASS), Madrid, Spain, 1–4 July 2019.
42. Bisin, R.; Paravan, C.; Alberti, S.; Galfetti, L. A new strategy for the reinforcement of paraffin-based fuels based on cellular structures: The armored grain—Mechanical characterization. *Acta. Astronaut.* **2020**, *176*, 494–509. [[CrossRef](#)]
43. Bisin, R.; Paravan, C.; Verga, A.; Galfetti, L. Towards High-Performing Paraffin-based Fuels Exploiting the Armored Grain Concept. In Proceedings of the 9th European Conference for Aeronautics and Space Sciences (EUCASS), Lille, France, 27 June–1 July 2022.
44. Bisin, R.; Paravan, C.; Parolini, S.; Galfetti, L. Impact of 3D-printing on the Mechanical Reinforcement and the Ballistic Response of Paraffin-based Fuels: The Armored Grain. In Proceedings of the AIAA Propulsion and Energy 2020 Forum, Virtual Event, 24–28 August 2020.
45. Bisin, R.; Paravan, C.; Alberti, S.; Galfetti, L. An Innovative Strategy for Paraffin-based Fuels Reinforcement: Part I, Mechanical and Pre-Burning Characterization. In Proceedings of the 8th European Conference for Aeronautics and Aerospace Sciences (EUCASS), Madrid, Spain, 1–4 July 2019.
46. Hill, C.; McDougall, C.C.; Messinger, T.; Johansen, C.T. Modification of Paraffin-based Hybrid Rocket Fuels Using Structural Lattices. In Proceedings of the AIAA Propulsion and Energy 2019 Forum, Indianapolis, IN, USA, 19–22 August 2019.
47. Hill, C.; Johansen, C.T. Evaluation of Lattice-Augmented Hybrid Rocket Fuels on a Slab Burner. In Proceedings of the AIAA Propulsion and Energy 2021 Forum, Virtual Event, 9–11 August 2021.
48. Lin, X.; Qu, D.; Chen, X.; Wang, Z.; Luo, J.; Meng, D.; Liu, G.; Zhang, K.; Li, F.; Wu, X. Three-dimensional printed metal-nested composite fuel grains with superior mechanical and combustion properties. *Virtual Phys. Prototy.* **2022**, *17*, 437–450. [[CrossRef](#)]
49. Wu, Y.; Zhang, Z.; Wang, W.; Wang, N. Combustion characteristics of skeleton polymer reinforced paraffin-wax fuel grain for applications in hybrid rocket motors. *Combust. Flame* **2022**, *241*, 112055. [[CrossRef](#)]
50. Lai, K.; Soria, J.; Atkinson, C. *ABS Infill Structures for Enhancing the Performance of Paraffin Fuel Grains in Hybrid Rocket Engines*; Technical Report LTRAC-TR 2022.1; Monash University: Melbourne, Australia, 2022.
51. Meier, J.; Reynolds, J.; Whalen, S.; Patel, J.; Bortner, M.J.; Young, G. Improved Hybrid Rocket Performance by Additively Manufactured Gel-Infused Solid Fuels. *J. Propuls. Power* **2023**, *39*, 97–105. [[CrossRef](#)]
52. Oztan, C.; Ginzburg, E.; Akin, M.; Zhou, Y.; Leblanc, R.M.; Coverstone, V. 3D printed ABS/paraffin hybrid rocket fuels with carbon dots for superior combustion performance. *Combust. Flame* **2021**, *225*, 428–434. [[CrossRef](#)]
53. Strategies for 3D Printing Advanced Hybrid Rocket Fuel Grains and Hybrid-Like Liquid Rocket Motors. Available online: <https://www.slideshare.net/JerryFuller3/strategies-for-3d-printing-advanced-hybrid-rocket-fuel-grains-and-hybridlike-liquid-rocket-motorsadditive-innovationfuller> (accessed on 20 February 2023).
54. McCulley, J.; Bath, A.; Whitmore, S. Design and Testing of FDM Manufactured Paraffin-ABS Hybrid Rocket Motors. In Proceedings of the 48th AIAA/ASME/SAE/ASEE Joint Propulsion Conference & Exhibit, Atlanta, GA, USA, 30 July–1 August 2012.
55. Aarant, T.; Bass, J.; Grizzel, T.; Holladay, S.; McVey, M.; Putthoff, W.; Shaw, A.; Tarle, P.; Nickel, R.; Littlel, C.; et al. The Development of a Powder-Filled, Abs Matric for Use as Fuel In A Hybrid Rocket Motor. In Proceedings of the AIAA Propulsion and Energy 2019 Forum, Indianapolis, IN, USA, 19–22 August 2019.
56. Holladay, S.; Aarant, T.; Bass, J.; Grizzel, T.; McVey, M.; Putthoff, W.; Shaw, A.; Littel, C.; Lyne, J.E. Hybrid Rocket Engine Design Utilizing a Polymer Matrix Encapsulating Pulverized Fuel. Undergraduate Thesis, University of Tennessee, Knoxville, TN, USA, 2019.
57. Barnhill, B.; Darling, S.; Springer, A.; Todd, A.; Whaley, S. *Design and Development of Hybrid Rocket for Spaceport America Cup*; University of Tennessee: Knoxville, TN, USA, 2019.
58. Bettella, A.; Lazzarin, M.; Bellomo, N.; Barato, F.; Pavarin, D.; Grosse, M. Testing and CFD Simulation of Diaphragm Hybrid Rocket Motors. In Proceedings of the 47th AIAA/ASME/SAE/ASEE Joint Propulsion Conference & Exhibit, San Diego, CA, USA, 31 July–3 August 2011.
59. Doran, E.; Dyer, J.; Lohner, K.; Dunn, Z.; Cantwell, B.; Zilliac, G. Nitrous Oxide Hybrid Rocket Motor Fuel Regression Rate Characterization. In Proceedings of the 43rd AIAA/ASME/SAE/ASEE Joint Propulsion Conference & Exhibit, Cincinnati, OH, USA, 8–11 July 2007.
60. Whitmore, S.A.; Olsen, K.C.; Forster, P.; Oztan, C.Y.; Coverstone, V.L. Test and Evaluation of Copper-Enhanced, 3-D Printed ABS Hybrid Rocket Fuels. In Proceedings of the AIAA Propulsion and Energy 2021 Forum, Virtual Event, 9–11 August 2021.
61. Okutani, Y.; Saito, Y.; Kimino, M.; Tsuji, A.; Soeda, K.; Nagata, H. Investigation of Regression Rate under High-Pressure in Axial-Injection End-Burning Hybrid Rockets. In Proceedings of the 2018 Joint Propulsion Conference, Cincinnati, OH, USA, 9–11 July 2018.
62. Saito, Y.; Yokoi, T.; Totani, T.; Wakita, M.; Nagata, H. Fuel Regression Characteristics of a Novel Axial-Injection End-Burning Hybrid Rocket. *J. Propuls. Power* **2018**, *34*, 247–259. [[CrossRef](#)]
63. Matsuoka, T.; Murakami, S.; Nagata, H. Transition characteristics of combustion modes for flame spread in solid fuel tube. *Combust. Flame* **2012**, *159*, 2466–2473. [[CrossRef](#)]
64. Fukada, M.; Suzuki, S.; Hayasaka, H.; Maebayashi, H.; Mungyu, S.; Leung, Y.A.M.; Nagata, H. Necessary Condition of Regression Mode in Axial-Injection End-burning Hybrid Rockets. In Proceedings of the AIAA SCITECH 2023 Forum, National Harbor, MD, USA, 23–27 January 2023.

65. Saito, Y.; Kimino, M.; Tsuji, A.; Okutani, Y.; Soeda, K.; Nagata, H. High Pressure Fuel Regression Fuel regression characteristics Characteristics of Axial-Injection End-Burning Hybrid Rockets. *J. Propuls. Power* **2019**, *35*, 328–341. [[CrossRef](#)]
66. Nagata, H.; Teraki, H.; Saito, Y.; Kanai, R.; Yasukochi, H.; Wakita, M.; Totani, T. Verification Firings of End-Burning Type Hybrid Rockets. *J. Propuls. Power* **2017**, *33*, 1473–1477. [[CrossRef](#)]
67. Okuda, R.; Komizu, K.; Tsuji, A.; Miwa, T.; Fukada, M.; Kamps, L.; Nagata, H. Fuel Regression Characteristics of Axial-Injection End-Burning Hybrid Rocket Using Nitrous Oxide. *J. Propuls. Power* **2022**, *38*, 759–770. [[CrossRef](#)]
68. Hitt, M.A.; Agnew, J.F. Printed Axial-Injection, End-Burning Hybrid Fuel Grain Study. *J. Spacecr. Rockets* **2021**, *58*, 1552–1556. [[CrossRef](#)]
69. Hitt, M.A. Preliminary Additively Manufactured Axial-Injection, End-Burning Hybrid Rocket Motor Regression Rate Study. In Proceedings of the 2018 Joint Propulsion Conference, Cincinnati, OH, USA, 9–11 July 2018.
70. Hitt, M.A. Additively Manufactured Axial-Injection, End-Burning Hybrid Motor Regression Rate Study. *J. Propuls. Power* **2020**, *36*, 485–487. [[CrossRef](#)]
71. Hirai, S.; Kamps, L.; Nobuhara, Y.; Nagata, H. Demonstration of Axial-Injection End-Burning Hybrid Rocket using FDM 3D Printer. In Proceedings of the AIAA SCITECH 2023 Forum, National Harbor, MD, USA, 23–27 January 2023.
72. Gordon, S.; McBride, B.J. *Computer Program for Calculation of Complex Chemical Equilibrium Compositions and Applications. Part I: Analysis*; NASA Reference Publication 1311-1: Cleveland, OH, USA, 1994.
73. Gordon, S.; McBride, B.J. *Computer Program for Calculation of Complex Chemical Equilibrium Compositions and Applications. Part II: Users Manual and Program Description*; NASA Reference Publication 1311-2: Cleveland, OH, USA, 1996.
74. Thomas, J.C.; Peterson, E.L. HTPB Heat of Formation: Literature Survey, Group Additive Estimations, and Theoretical Effects. *AIAA J.* **2022**, *60*, 1269–1282. [[CrossRef](#)]
75. Ahn, B.; Huh, J.; Bhosale, V.K.; Kwon, S. Three-Dimensionally Printed Polylactic Acid as Solid Fuel for Hydrogen Peroxide Hybrid Rockets. *J. Propuls. Power* **2021**, *29*, 582–592. [[CrossRef](#)]
76. Zheng, W.R.; Li, S.F.; Chow, W.K. Review on Chemical Reactions of Burning Poly(methyl methacrylate) PMMA. *J. Fire Sci.* **2002**, *20*, 401–433. [[CrossRef](#)]
77. Joshi, R.M.; Zwolinski, B.J. Heats of Combustion Studies on Polymers. *Macromolecules* **1968**, *1*, 25–30. [[CrossRef](#)]
78. Herps, H.H.T. Modelling and Comparative Assessment of Polyamide-6 Manufacturing towards a Sustainable Chemical Industry. Ph.D. Thesis, Utrecht University, Utrecht, The Netherlands, 2020.
79. Lyon, R.E. *Solid-State Thermochemistry of Flaming Combustion*; DOT/FAA/AR-99/56, ADA367981; Office of Aviation: Washington, DC, USA, 1999.
80. Walters, R.N.; Hackett, S.M.; Lyon, R.E. Heats of Combustion of High Temperature Polymers. *Fire Mater.* **2000**, *24*, 209–252. [[CrossRef](#)]
81. Walters, R.N. Molar Group Contributions to the Heat of Combustion. *Fire Mater.* **2002**, *26*, 103–145. [[CrossRef](#)]
82. Walters, R.N.; Lyon, R.E. Molar Group Contributions to Polymer Flammability. *J. Appl. Polym. Sci.* **2003**, *87*, 548–563. [[CrossRef](#)]
83. Heister, S.; Wernimont, E. Chapter 11: Hydrogen Peroxide, Hydroxyl Ammonium Nitrate, and Other Storable Oxidizers. In *Fundamentals of Hybrid Rocket Combustion and Propulsion*; Kuo, K.K., Chiaverini, M., Eds.; American Institute of Aeronautics and Astronautics, Inc.: Reston, VA, USA, 2007; Volume 218, pp. 457–488.

Disclaimer/Publisher’s Note: The statements, opinions and data contained in all publications are solely those of the individual author(s) and contributor(s) and not of MDPI and/or the editor(s). MDPI and/or the editor(s) disclaim responsibility for any injury to people or property resulting from any ideas, methods, instructions or products referred to in the content.